

# ELASTIC CHIRAL WAVEGUIDES WITH GYRO-HINGES

by G. CARTA<sup>†</sup>

(Mechanical Engineering and Materials Research Centre, Liverpool John Moores University, Byrom Street, Liverpool L3 3AF)

M. J. NIEVES

(School of Computing and Mathematics, Keele University, The Covert, Keele ST5 5BG and Department of Mechanical, Chemical and Material Engineering, University of Cagliari, Piazza d'Armi, Cagliari 09123, Italy)

I. S. JONES

(Mechanical Engineering and Materials Research Centre, Liverpool John Moores University, Byrom Street, Liverpool L3 3AF)

N. V. MOVCHAN and A. B. MOVCHAN

(Department of Mathematical Sciences, University of Liverpool, Peach Street, Liverpool L69 7ZL)

[Received 18 October 2017. Revise 12 January 2018. Accepted 17 January 2018]

## Summary

This article presents a novel chiral structure, consisting of Euler–Bernoulli beams connected to gyroscopic spinners. A new type of boundary condition is introduced, which is referred to as a *gyro-hinge*. In this system, flexural waves are coupled with rotational motion. Time-harmonic conditions are derived by assuming small nutation angles of the spinners. It is shown that the eigenfrequencies of a finite beam with gyro-hinges at one or both ends change dramatically with the moments of inertia and the spin and precession rates of the spinners. The formulation is then extended to elastic beams with periodically-spaced gyro-hinges, whose dispersion properties are investigated in detail. In particular, it is shown how stop-bands and standing modes are affected by the introduction of gyroscopic spinners at the junctions. It is also demonstrated that a periodic system composed of beams connected by gyro-hinges represents a good approximation of a *gyrobeam*, a theoretical structural element consisting of an elastic beam possessing a continuous distribution of stored angular momentum. The gyricity coefficient of a gyrobeam is then interpreted in terms of the physical parameters of the system of beams with gyroscopic spinners. This article opens a new perspective on the design and practical implementation of chiral mechanical systems.

## 1. Introduction

Chiral elastic systems have attracted increasing interest from the research community in recent years, due to their special dynamic properties. According to the original definition (1), an object or a geometrical figure is ‘chiral’ if it cannot be superimposed onto its mirror image. Chirality has been exploited to design auxetic materials (2, 3) and to alter the dispersive properties of lattice structures (4, 5). A continuous medium with chiral resonators was studied in (6) as a filtering and focussing

---

<sup>†</sup><G.carta@ljmu.ac.uk>

device. A chiral beam with multiple resonators was proposed in (7) to achieve broadband vibration attenuation. More recently, a doubly-periodic chiral lattice with tilted resonators was designed in (8, 9), where it was shown that pressure and shear waves are coupled. Localisation and directional preference of waves were observed.

In an elastic discrete medium, chirality can be induced and controlled by attaching a system of gyroscopic spinners. The model of a gyro-elastic lattice was first proposed in (10), where it was used as a cloaking device to hide an object in a two-dimensional environment. Polarisation of waves, high-frequency anisotropy and dynamic response under an external excitation of a gyro-elastic lattice were analysed in (11). Gyroscopic spinners can also be employed to generate edge waves propagating in one direction, as shown in the experimental work (12) and in the numerical investigation (13). A localised unidirectional wave pattern can be created in an elastic lattice by introducing a non-uniform system of gyroscopic spinners, as demonstrated in (14), where it was also shown that the unidirectional wave can be diverted by changing the arrangement of the spinners within the medium.

The aim of the present article is to investigate the effect of gyroscopic spinners on the dynamics of flexural systems. Numerous studies have been dedicated to periodic flexural structures in recent decades (15)–(26). The notion of ‘gyro-elastic beam’ (or ‘gyrobeam’), which represents an elastic beam with a continuous distribution of stored angular momentum, was introduced in (27). The theory of gyro-elastic continua was developed in (27)–(29), where special attention was given to eigenvalue problems of gyrobeams. Static and dynamic instabilities displayed by gyro-elastic beams were analysed in (30). The formulation of micropolar gyroelastic continua, based on asymmetric Cosserat elasticity theory, was presented in (31, 32). In terms of practical applications, it has been recently shown that gyrobeams can be employed to create wide low-frequency band-gaps if connected to a civil engineering structure, such as a bridge (33); the seismic protection design based on the use of gyrobeams offers an efficient alternative to the installation of high-contrast resonators (34).

The theory of gyro-elastic beams is based on an elegant formulation, but it presents a serious drawback for the purpose of practical construction: the gyricity parameter appearing in the equations of motion is not defined in terms of physical quantities. This makes it impossible to construct a gyrobeam in practice. In this article, we offer a novel design of a gyro-elastic beam, consisting of an elastic beam with gyro-hinges. A gyro-hinge is realised by attaching a gyroscopic spinner to a pinned support of the beam. This structural element exhibits chiral properties, which are similar to those observed in a gyrobeam, such as a splitting of eigenfrequencies and a coupling between flexural and rotational motion (33).

The article is organised as follows: in section 2, we present the equations of motion of the gyroscopic spinner and the elastic beam in the transient regime. In section 3, we formulate the gyro-hinge boundary conditions, and we present their form when the motion is time-harmonic. In section 4, we determine the eigenfrequencies and eigenmodes of a finite beam with a gyro-hinge at one end and various boundary conditions at the other end. In section 5, we discuss the results for a specific case, namely when the gyroscopic spinner has a cylindrical shape. In section 6, we study Floquet–Bloch waves in a periodic structure composed of Euler–Bernoulli beams connected by gyro-hinges. In section 7, we compare the dispersive properties of that periodic system with the dispersive properties of a periodic structure made of gyrobeams connected by classical hinges; furthermore, we give an interpretation of the gyricity parameter in the equations of motion of a gyrobeam in terms of the physical parameters of the system of beams with gyroscopic spinners. In section 8 we provide concluding remarks. Finally, in Appendix A we discuss the eigenvalue problem for the special case of a massless beam connected to a gyro-hinge.

## 2. Formulation of the problem

We consider an Euler–Bernoulli beam, shown in Fig. 1a, clamped at one end (point A) and connected to a gyroscopic spinner at the other end (point B). At the point B, the displacements of the beam and of the spinner are zero, and the spinner axis is assumed to coincide with the tangent line to the deformed shape of the beam. In addition, the connection between the spinner and the beam at the junction point B is such that the spinning motion of the spinner is not transmitted to the beam. Hence the beam does not spin around its own axis.

### 2.1 Governing equations for the gyroscopic spinner

The Cartesian coordinate system  $B\xi\eta\zeta$  in Fig. 1b represents the principal reference frame of the gyroscopic spinner, which rotates around the fixed point B. The angles  $\theta$ ,  $\phi$  and  $\psi$  denote the angles of nutation, precession and spin, respectively. We assume that the principal reference frame does not rotate around the principal  $\zeta$ -axis, since the beam does not spin around its own axis. Accordingly, with the reference to Fig. 1b, the angular velocity

$$\boldsymbol{\omega} = \omega_\xi \mathbf{e}_\xi + \omega_\eta \mathbf{e}_\eta + \omega_\zeta \mathbf{e}_\zeta$$

of the gyroscope can be expressed in terms of the Euler's angles  $\theta$ ,  $\phi$ ,  $\psi$  as

$$\omega_\xi = \dot{\theta}, \quad \omega_\eta = \dot{\phi} \sin(\theta), \quad \omega_\zeta = \dot{\phi} \cos(\theta) + \dot{\psi}, \quad (2.1)$$

which follows from (4.87) of (35). Here the dot represents derivative with respect to time. Similarly, for the non-spinning frame associated with the axes  $(\xi, \eta, \zeta)$  we define the angular velocity vector  $\tilde{\boldsymbol{\omega}}$  with components  $\tilde{\omega}_\xi$ ,  $\tilde{\omega}_\eta$ ,  $\tilde{\omega}_\zeta$  such that

$$\tilde{\boldsymbol{\omega}} = \tilde{\omega}_\xi \mathbf{e}_\xi + \tilde{\omega}_\eta \mathbf{e}_\eta + \tilde{\omega}_\zeta \mathbf{e}_\zeta$$

and

$$\tilde{\omega}_\xi = \omega_\xi, \quad \tilde{\omega}_\eta = \omega_\eta, \quad \tilde{\omega}_\zeta = \dot{\phi} \cos(\theta). \quad (2.2)$$

The equations of motion for the spinner in the principal reference frame  $B\xi\eta\zeta$  are then given by (35)

$$\mathbf{M} = I_0 \dot{\omega}_\xi \mathbf{e}_\xi + I_0 \dot{\omega}_\eta \mathbf{e}_\eta + I \dot{\omega}_\zeta \mathbf{e}_\zeta + \tilde{\boldsymbol{\omega}} \times \mathbf{L}, \quad (2.3)$$

where

$$\mathbf{L} = I_0 \omega_\xi \mathbf{e}_\xi + I_0 \omega_\eta \mathbf{e}_\eta + I \omega_\zeta \mathbf{e}_\zeta$$

is the vector of angular momentum of the spinner, which is assumed to be a solid of revolution around the  $\zeta$ -axis whose moments of inertia with respect to the principal axes are  $I_\xi = I_\eta = I_0$  and  $I_\zeta = I$ , while

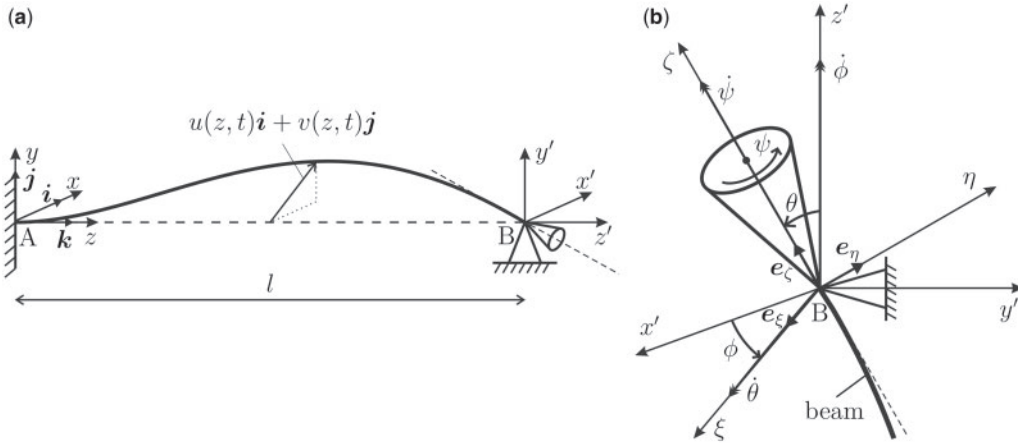
$$\mathbf{M} = M_\xi \mathbf{e}_\xi + M_\eta \mathbf{e}_\eta + M_\zeta \mathbf{e}_\zeta$$

is the vector of moments applied to the spinner. The components of  $\mathbf{M}$  take the form

$$M_\xi = I_0 \dot{\omega}_\xi + I \omega_\eta \omega_\zeta - I_0 \omega_\eta \tilde{\omega}_\zeta, \quad (2.4a)$$

$$M_\eta = I_0 \dot{\omega}_\eta + I_0 \omega_\xi \tilde{\omega}_\zeta - I \omega_\xi \omega_\zeta, \quad (2.4b)$$

$$M_\zeta = I \dot{\omega}_\zeta. \quad (2.4c)$$



**Fig. 1** (a) Euler–Bernoulli beam with a clamped end at  $z = 0$  and a gyro-hinge at  $z = l$ ; (b) representation of a gyroscopic spinner, where  $\psi$ ,  $\phi$  and  $\theta$  are the angles of spin, precession and nutation, respectively

The vector of moments  $\mathbf{M}$  can be written as

$$\mathbf{M} = (M_\xi, M_\eta, M_\zeta)^\top = \mathbf{R}\mathbf{M}' = \mathbf{R} (M_{x'}, M_{y'}, M_{z'})^\top, \quad (2.5)$$

where  $\mathbf{R}$  is the rotation matrix,

$$\mathbf{R} = \begin{pmatrix} \cos(\phi) & \sin(\phi) & 0 \\ -\cos(\theta)\sin(\phi) & \cos(\theta)\cos(\phi) & \sin(\theta) \\ \sin(\theta)\sin(\phi) & -\sin(\theta)\cos(\phi) & \cos(\theta) \end{pmatrix}, \quad (2.6)$$

and  $\mathbf{B}x'y'z'$  is the fixed Cartesian coordinate system, aligned with the axes  $x$ ,  $y$  and  $z$  and centered at  $B$  (see Fig. 1). By using (2.1)–(2.6), the moments (2.4) acting on the gyroscopic spinner can be re-written in the fixed frame. Accordingly, the equations of motion are expressed by

$$\cos(\phi)M_{x'} + \sin(\phi)M_{y'} = I_0\ddot{\theta} + (I - I_0)\dot{\phi}^2 \sin(\theta)\cos(\theta) + I\dot{\phi}\dot{\psi}\sin(\theta), \quad (2.7a)$$

$$-\cos(\theta)\sin(\phi)M_{x'} + \cos(\theta)\cos(\phi)M_{y'} + \sin(\theta)M_{z'} \quad (2.7b)$$

$$= I_0[\ddot{\phi}\sin(\theta) + \dot{\phi}\dot{\theta}\cos(\theta)] - (I - I_0)\dot{\theta}\dot{\phi}\cos(\theta) - I\dot{\theta}\dot{\psi},$$

$$\sin(\theta)\sin(\phi)M_{x'} - \sin(\theta)\cos(\phi)M_{y'} + \cos(\theta)M_{z'} = I\frac{d}{dt}[\dot{\phi}\cos(\theta) + \dot{\psi}]. \quad (2.7c)$$

We assume that the nutation angle is small ( $\theta \ll 1$ ). In this case, after linearising with respect to  $\theta$  and its derivatives, (2.7) to the leading order take the form:

$$M_{x'} = \sin(\phi)[(I - 2I_0)\dot{\phi} + I\dot{\psi}]\dot{\theta} + I_0\cos(\phi)\ddot{\theta} + \left\{ (I - I_0)[\dot{\phi}^2\cos(\phi) + \ddot{\phi}\sin(\phi)] + I[\dot{\phi}\dot{\psi}\cos(\phi) + \ddot{\psi}\sin(\phi)] \right\}\theta, \quad (2.8a)$$

$$M_{y'} = -\cos(\phi) \left[ (I - 2I_0) \dot{\phi} + I \dot{\psi} \right] \dot{\theta} + I_0 \sin(\phi) \ddot{\theta} + \left\{ (I - I_0) \left[ \dot{\phi}^2 \sin(\phi) - \ddot{\phi} \cos(\phi) \right] + I \left[ \dot{\phi} \dot{\psi} \sin(\phi) - \ddot{\psi} \cos(\phi) \right] \right\} \theta, \quad (2.8b)$$

$$M_{z'} = I \frac{d}{dt} (\dot{\phi} + \dot{\psi}). \quad (2.8c)$$

The quantity  $\Omega = \dot{\phi} + \dot{\psi}$  will be referred to as the *gyricity* of the system. It is noted that the gyricity has contributions from both the precession rate and the spin rate of the gyroscopic spinner.

## 2.2 Governing equations for the beam

The equations of motion for an Euler–Bernoulli beam in the transient regime are given by

$$EJ \frac{\partial^4 u}{\partial z^4} + \rho \mathcal{A} \frac{\partial^2 u}{\partial t^2} = 0, \quad (2.9a)$$

$$EJ \frac{\partial^4 v}{\partial z^4} + \rho \mathcal{A} \frac{\partial^2 v}{\partial t^2} = 0, \quad (2.9b)$$

where  $t$  is time ( $t \geq 0$ ),  $z$  is the direction of the beam axis in the undeformed configuration ( $0 \leq z \leq l$ ),  $u = u(z, t)$  and  $v = v(z, t)$  are the components of the transverse displacement of the beam (see Fig. 1a),  $E$  is the Young's modulus,  $\rho$  is the density,  $\mathcal{A}$  is the cross-sectional area and  $J$  is the second moment of area, which is assumed to be the same with respect to the  $x$ - and  $y$ -direction ( $J = J_x = J_y$ ) for simplicity. We point out that we do not study the longitudinal motion of the beam, whose governing equations are decoupled from (2.9) under the assumption of small displacements.

## 3. The boundary conditions for the gyro-hinge

At the junction point, the beam and the gyroscopic spinner have zero displacements and identical rotations with respect to the  $x$ - and  $y$ -axis. The conditions for continuity of slope are expressed in the reference system of Fig. 1a as

$$\left. \frac{\partial u}{\partial z} \right|_{z=l} = u'_l = \theta \sin(\phi), \quad (3.1a)$$

$$\left. \frac{\partial v}{\partial z} \right|_{z=l} = v'_l = -\theta \cos(\phi), \quad (3.1b)$$

where  $l$  is the length of the beam.

The boundary conditions at  $z = l$  for the bending moments of the beam become

$$M_{x'} = EJ \left. \frac{\partial^2 v}{\partial z^2} \right|_{z=l} = EJv''_l, \quad (3.2a)$$

$$M_{y'} = -EJ \left. \frac{\partial^2 u}{\partial z^2} \right|_{z=l} = -EJu''_l, \quad (3.2b)$$

where  $M_{x'}$  and  $M_{y'}$  are given in (2.8a) and (2.8b), respectively. We note that the bending moments in the beam at  $z = l$  are equal and opposite to the bending moments acting on the gyroscopic spinner. Assuming zero twisting moment in the beam, (2.8c) leads to

$$I \frac{d}{dt}(\dot{\phi} + \dot{\psi}) = M_{z'} = 0 \quad \Rightarrow \quad \dot{\phi} + \dot{\psi} = \Omega = \text{Const.} \quad (3.3)$$

Differentiating (3.1) twice with respect to time and using system (3.2) at  $z = l$ , (2.8a) and (2.8b) yield

$$u_l'' = -\frac{I_0}{EJ} \ddot{u}_l' - \frac{I\Omega}{EJ} \dot{v}_l', \quad (3.4a)$$

$$v_l'' = \frac{I\Omega}{EJ} \dot{u}_l' - \frac{I_0}{EJ} \ddot{v}_l'. \quad (3.4b)$$

The equations above will be referred to as *gyro-hinge boundary conditions*. It is apparent that the two boundary conditions are coupled and the coupling terms are each proportional to the gyricity  $\Omega$ . The coupling terms representing the gyroscopic action are also proportional to  $I$  and are independent of  $I_0$ .

It is interesting to note the following limiting cases:

- (i) When  $I = I_0 = 0$ , the curvatures  $u_l''$  and  $v_l''$  are zero and the gyro-hinge behaves as a classical hinge.
- (ii) When the gyroscopic spinner is both not spinning and not precessing, that is  $\Omega = 0$ , then the cross terms in (3.4) vanish and the gyroscopic spinner behaves as a solid with moment of inertia  $I_0$ . In this case, each curvature component of the beam at the end depends only on the corresponding rotation component at that end.

The above limiting cases will be further discussed in more detail in sections 4 and 5, when analysing specific examples.

### 3.1 Time-harmonic regime for gyro-hinge boundary conditions

In the time-harmonic regime, the displacement components of the beam are expressed by

$$u(z, t) = U(z)e^{i\omega t}, \quad (3.5a)$$

$$v(z, t) = V(z)e^{i\omega t}, \quad (3.5b)$$

where  $\omega$  is the radian frequency. Consequently, conditions (3.4) take the following matrix form:

$$\begin{pmatrix} U_l'' \\ V_l'' \end{pmatrix} = \begin{pmatrix} \frac{I_0}{EJ} \omega^2 & -i\omega \frac{I\Omega}{EJ} \\ i\omega \frac{I\Omega}{EJ} & \frac{I_0}{EJ} \omega^2 \end{pmatrix} \begin{pmatrix} U_l' \\ V_l' \end{pmatrix}. \quad (3.6)$$

The *time-harmonic gyro-hinge boundary conditions* (3.6) show how the curvatures in the beam at the junction point ( $U_l''$  and  $V_l''$ ) depend on the following quantities:

- the rotations of the beam at the junction point ( $U_l'$  and  $V_l'$ );

- the radian frequency of the vibrations of the beam ( $\omega$ );
- the flexural stiffness of the beam ( $EJ$ );
- the principal moments of inertia of the spinner ( $I$  and  $I_0$ ); and
- the gyricity  $\Omega$ .

We note the special case of  $\mathcal{D} = \omega^2 - (I/I_0)^2 \Omega^2 = 0$ , when the matrix in the right-hand side of (3.6) is degenerate. Given  $\Omega$ , this defines an eigenfrequency  $\omega$  of a linearised gyroscopic spinner. In this case, we also note that  $U_i'' = \pm iV_i''$ .

When  $I, I_0 \rightarrow \infty$  and the matrix on the right-hand side of (3.6) is non-degenerate, the rotations  $U_i', V_i' \rightarrow 0$ . In this case, the gyro-hinge behaves as a clamped end.

#### 4. Analytical results for vibrating beams with gyro-hinges

In this section, we determine the eigenfrequencies and eigenmodes of finite Euler–Bernoulli beams with a variety of different boundary conditions at the end  $z = 0$  and with a gyro-hinge at the end  $z = l$ . The results derived below are summarised in Fig. 2.

The governing equations for an Euler–Bernoulli beam in the time-harmonic regime are found by substituting the expressions (3.5) into the equations of motion (2.9):

$$\frac{d^4 U}{dz^4} - \beta^4 U = 0, \quad (4.1a)$$

$$\frac{d^4 V}{dz^4} - \beta^4 V = 0, \quad (4.1b)$$

where  $\beta = (\rho A \omega^2 / EJ)^{1/4}$  is the frequency-like parameter. The general solutions of (4.1) are given by

$$U(z) = A_1 \cos(\beta z) + A_2 \sin(\beta z) + A_3 \cosh(\beta z) + A_4 \sinh(\beta z), \quad (4.2a)$$

$$V(z) = B_1 \cos(\beta z) + B_2 \sin(\beta z) + B_3 \cosh(\beta z) + B_4 \sinh(\beta z). \quad (4.2b)$$


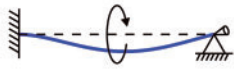



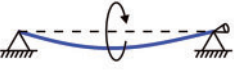



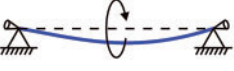


The coefficients  $A_i$  and  $B_i$  ( $1 \leq i \leq 4$ ) in the preceding expressions are determined from the boundary conditions. In particular, the gyro-hinge boundary conditions will lead to coupling of  $U$  and  $V$ .

##### 4.1 Beam with a clamped end and a gyro-hinge

We start by studying the beam sketched in Fig. 1a, which has a clamped end at  $z = 0$  and a gyro-hinge at  $z = l$ . The boundary conditions are given by

$$\begin{pmatrix} U \\ V \end{pmatrix} \Big|_{z=0} = \begin{pmatrix} U' \\ V' \end{pmatrix} \Big|_{z=0} = \begin{pmatrix} 0 \\ 0 \end{pmatrix}, \quad (4.3a)$$

$$\begin{pmatrix} U \\ V \end{pmatrix} \Big|_{z=l} = \begin{pmatrix} 0 \\ 0 \end{pmatrix}, \quad \begin{pmatrix} U'' \\ V'' \end{pmatrix} \Big|_{z=l} = \begin{pmatrix} \frac{I_0}{EJ} \omega^2 & -i\omega \frac{I\Omega}{EJ} \\ i\omega \frac{I\Omega}{EJ} & \frac{I_0}{EJ} \omega^2 \end{pmatrix} \begin{pmatrix} U' \\ V' \end{pmatrix} \Big|_{z=l}. \quad (4.3b)$$

		
eigenfrequency equation	first eigenmode	limits
<p>Eq. (4.4):</p> $(EJ)^2 \beta^2 [\sin(\beta l) \cosh(\beta l) - \cos(\beta l) \sinh(\beta l)]^2 - 2EJI_0 \beta \omega^2 [1 - \cos(\beta l) \cosh(\beta l)] \times [\sin(\beta l) \cosh(\beta l) - \cos(\beta l) \sinh(\beta l)] + \omega^2 (I_0^2 \omega^2 - I^2 \Omega^2) [1 - \cos(\beta l) \cosh(\beta l)]^2 = 0$		<p><math>I = I_0 = 0</math></p>  <p><math>I, I_0 \rightarrow \infty, \mathcal{D} \neq 0</math></p> 
		
eigenfrequency equation	first eigenmode	limits
<p>Eq. (4.10):</p> $4(EJ)^2 \beta^2 [\sin(\beta l) \sinh(\beta l)]^2 + 4EJI_0 \beta \omega^2 \times [\cos(\beta l) \sinh(\beta l) - \sin(\beta l) \cosh(\beta l)] \sin(\beta l) \sinh(\beta l) + \omega^2 (I_0^2 \omega^2 - I^2 \Omega^2) [\cos(\beta l) \sinh(\beta l) - \sin(\beta l) \cosh(\beta l)]^2 = 0$		<p><math>I = I_0 = 0</math></p>  <p><math>I, I_0 \rightarrow \infty, \mathcal{D} \neq 0</math></p> 
		
eigenfrequency equation	first eigenmode	limits
<p>Eq. (4.12):</p> $4(EJ)^4 \beta^4 [\sin(\beta l) \sinh(\beta l)]^2 - 4(EJ)^2 \beta^2 \omega^2 \sin(\beta l) \sinh(\beta l) \times \{ I_0^2 \omega^2 [2 \cos(\beta l) \cosh(\beta l) - 1] - I^2 \Omega^2 - 2EJI_0 \beta [\cos(\beta l) \sinh(\beta l) - \cosh(\beta l) \sin(\beta l)] \} + \omega^2 (I_0^2 \omega^2 - I^2 \Omega^2) \{ 2EJI_0 \beta \omega^2 \times [\cosh^2(\beta l) \sin(2\beta l) - 2 \cosh(\beta l) \sin(\beta l) + 2 \sinh(\beta l) \cos(\beta l) - \cos^2(\beta l) \sinh(2\beta l)] + \omega^2 (I_0^2 \omega^2 - I^2 \Omega^2) [1 - \cos(\beta l) \cosh(\beta l)]^2 + (EJ)^2 \beta^2 [2 \cosh(2\beta l) - 2 \cos(2\beta l) - \sin(2\beta l) \sinh(2\beta l)] \} = 0.$		<p><math>I = I_0 = 0</math></p>  <p><math>I, I_0 \rightarrow \infty, \mathcal{D} \neq 0</math></p> 

**Fig. 2** Euler–Bernoulli beams with a variety of different boundary conditions analysed in section 4. For each case, the equation providing the eigenfrequencies is shown in the left column, the first eigenmode is illustrated in the middle column and the limiting cases are indicated in the right column



Substituting the general solutions (4.2) into the boundary conditions (4.3) and looking for non-trivial solutions, we derive the following equation:

$$\begin{aligned} & (EJ)^2 \beta^2 [\sin(\beta l) \cosh(\beta l) - \cos(\beta l) \sinh(\beta l)]^2 \\ & - 2EJI_0 \beta \omega^2 [1 - \cos(\beta l) \cosh(\beta l)] [\sin(\beta l) \cosh(\beta l) - \cos(\beta l) \sinh(\beta l)] \\ & + \omega^2 (I_0^2 \omega^2 - I^2 \Omega^2) [1 - \cos(\beta l) \cosh(\beta l)]^2 = 0. \end{aligned} \quad (4.4)$$

The solutions of (4.4) are the eigenfrequencies of the beam in Fig. 1a. They will be presented in section 5.1 as functions of the ratio  $I/I_0$  and of the gyricity  $\Omega$ . The eigenfrequencies obtained for some limiting values of the moments of inertia of the spinner are discussed below.

4.1.1 Special cases. If the gyroscopic spinner is removed, that is  $I = I_0 = 0$ , Eq. (4.4) becomes

$$[\sin(\beta l) \cosh(\beta l) - \cos(\beta l) \sinh(\beta l)]^2 = 0, \quad (4.5)$$

which is the well-known equation for the eigenfrequencies of a clamped-hinged beam when the two second moments of area of the cross-section are identical (36). From (4.5) it is apparent that each eigenfrequency has multiplicity 2.

When the gyroscopic spinner is both not spinning and not precessing ( $\Omega = 0$ ), (4.4) simplifies as follows:

$$\left\{ EJ\beta [\sin(\beta l) \cosh(\beta l) - \cos(\beta l) \sinh(\beta l)] - I_0 \omega^2 [1 - \cos(\beta l) \cosh(\beta l)] \right\}^2 = 0. \quad (4.6)$$

The solutions of (4.6) are the double eigenfrequencies of a clamped-hinged beam, with a mass of rotational inertia  $I_0$  attached to the hinged end.

When  $I$  is sufficiently large so that the coefficient  $I^2 \Omega^2 \omega^2$  is dominant compared to all other coefficients in (4.4), to leading order we retrieve the following equation:

$$[1 - \cos(\beta l) \cosh(\beta l)]^2 = 0, \quad (4.7)$$

which provides the eigenfrequencies of a beam with both ends clamped (36). Accordingly, in the latter case we expect double eigenfrequencies, given by the solutions of (4.7), and eigenmodes resembling those of a clamped-clamped beam.

When  $\omega^2 = (I/I_0)^2 \Omega^2$ , Eq. (4.4) takes the form

$$\begin{aligned} & EJ\beta [\sin(\beta l) \cosh(\beta l) - \cos(\beta l) \sinh(\beta l)] \\ & \times \left\{ EJ\beta [\sin(\beta l) \cosh(\beta l) - \cos(\beta l) \sinh(\beta l)] - 2I_0 \omega^2 [1 - \cos(\beta l) \cosh(\beta l)] \right\} = 0. \end{aligned} \quad (4.8)$$

In this case, one eigenfrequency is identical to the natural frequency of a clamped-hinged beam (see (4.5)), while the other one coincides with the eigenfrequency of a clamped-hinged beam connected to a mass with rotational inertia  $2I_0$  at the hinged end (see (4.6)).

#### 4.2 Beam with a classical hinge and a gyro-hinge

Now we consider a beam with a classical hinge at  $z = 0$  and a gyro-hinge at  $z = l$ . The boundary conditions at  $z = 0$  are expressed by

$$\begin{pmatrix} U \\ V \end{pmatrix} \Big|_{z=0} = \begin{pmatrix} U'' \\ V'' \end{pmatrix} \Big|_{z=0} = \begin{pmatrix} 0 \\ 0 \end{pmatrix}, \quad (4.9)$$

while those at  $z = l$  are given by (4.3b). For non-trivial solutions of (4.9) and (4.3b) to exist, the following identity must hold, which provides the eigenfrequencies of the beam:

$$\begin{aligned} & 4(EJ)^2 \beta^2 [\sin(\beta l) \sinh(\beta l)]^2 \\ & + 4EJI_0 \beta \omega^2 [\cos(\beta l) \sinh(\beta l) - \sin(\beta l) \cosh(\beta l)] \sin(\beta l) \sinh(\beta l) \\ & + \omega^2 (I_0^2 \omega^2 - I^2 \Omega^2) [\cos(\beta l) \sinh(\beta l) - \sin(\beta l) \cosh(\beta l)]^2 = 0. \end{aligned} \quad (4.10)$$

The eigenfrequencies of the beam versus each of the ratio  $I/I_0$  and the gyricity  $\Omega$  will be discussed in section 5.2.

#### 4.3 Beam with two gyro-hinges

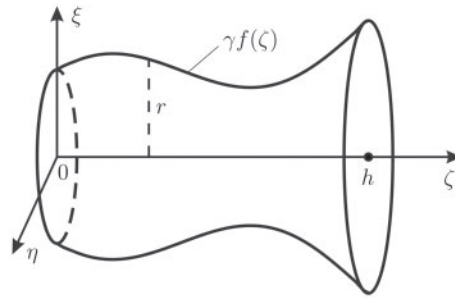
Finally in this section, we consider a beam with identical gyro-hinges at both ends. The boundary conditions for this structural element at  $z = 0$  are given by

$$\begin{pmatrix} U \\ V \end{pmatrix} \Big|_{z=0} = \begin{pmatrix} 0 \\ 0 \end{pmatrix}, \quad \begin{pmatrix} U'' \\ V'' \end{pmatrix} \Big|_{z=0} = \begin{pmatrix} -\frac{I_0}{EJ} \omega^2 & i\omega \frac{I\Omega}{EJ} \\ -i\omega \frac{I\Omega}{EJ} & -\frac{I_0}{EJ} \omega^2 \end{pmatrix} \begin{pmatrix} U' \\ V' \end{pmatrix} \Big|_{z=0}. \quad (4.11)$$

Similar conditions hold at  $z = l$  (see (4.3b)). This yields the following form of the eigenfrequency equation:

$$\begin{aligned} & 4(EJ)^4 \beta^4 [\sin(\beta l) \sinh(\beta l)]^2 - 4(EJ)^2 \beta^2 \omega^2 \sin(\beta l) \sinh(\beta l) \\ & \times \left\{ I_0^2 \omega^2 [2 \cos(\beta l) \cosh(\beta l) - 1] - I^2 \Omega^2 - 2EJI_0 \beta [\cos(\beta l) \sinh(\beta l) - \cosh(\beta l) \sin(\beta l)] \right\} \\ & + \omega^2 (I_0^2 \omega^2 - I^2 \Omega^2) \left\{ 2EJI_0 \beta \omega^2 [\cosh^2(\beta l) \sin(2\beta l) - 2 \cosh(\beta l) \sin(\beta l) \right. \\ & \left. + 2 \sinh(\beta l) \cos(\beta l) - \cos^2(\beta l) \sinh(2\beta l)] + \omega^2 (I_0^2 \omega^2 - I^2 \Omega^2) [1 - \cos(\beta l) \cosh(\beta l)]^2 \right. \\ & \left. + (EJ)^2 \beta^2 [2 \cosh(2\beta l) - 2 \cos(2\beta l) - \sin(2\beta l) \sinh(2\beta l)] \right\} = 0. \end{aligned} \quad (4.12)$$

The eigenfrequencies of a beam with two gyro-hinges will be discussed in section 5.3. Additionally, special attention will be given to the study of the limiting values of the eigenfrequencies, which allow us to predict the ranges of eigenfrequencies for each vibration mode that vary with the parameters of the spinner.



**Fig. 3** Generic shape for the gyroscopic spinner, represented by a solid of revolution around the  $\zeta$ -axis

### 5. Cylindrical gyroscopic spinner

In this section, we assume that the gyroscopic spinner is a cylinder with radius  $r_{\text{cyl}}$ , height  $h_{\text{cyl}}$ , density  $\rho_{\text{cyl}}$  and mass  $m_{\text{cyl}} = \rho_{\text{cyl}} \pi r_{\text{cyl}}^2 h_{\text{cyl}}$ . The principal moments of inertia of the cylindrical spinner and their ratio are given by

$$I = m_{\text{cyl}} \frac{r_{\text{cyl}}^2}{2}, \quad I_0 = m_{\text{cyl}} \left( \frac{r_{\text{cyl}}^2}{4} + \frac{h_{\text{cyl}}^2}{3} \right) \quad \text{and} \quad \frac{I}{I_0} = \frac{6r_{\text{cyl}}^2}{3r_{\text{cyl}}^2 + 4h_{\text{cyl}}^2}, \quad (5.1)$$

respectively. In the calculations, we fix the height  $h_{\text{cyl}}$  and we consider different values of the radius from  $r_{\text{cyl}} = 0$  to  $r_{\text{cyl}} \rightarrow \infty$ . We note that  $I/I_0 = 0$  when  $r_{\text{cyl}} = 0$  and  $I/I_0 \rightarrow 2$  in the limit when  $r_{\text{cyl}} \rightarrow \infty$ .

**REMARK:** The limiting cases above can also be considered for a generic shape of a solid of revolution. To illustrate this, we assume that the spinner is the solid defined in cylindrical coordinates as follows:

$$\zeta \in [0, h], \quad 0 \leq r \leq \gamma f(\zeta), \quad (5.2)$$

where  $f$  is a bounded function on  $[0, h]$ , and  $\gamma$  is a positive parameter (see Fig. 3). The moments of inertia  $I$  and  $I_0$  have the form (37)

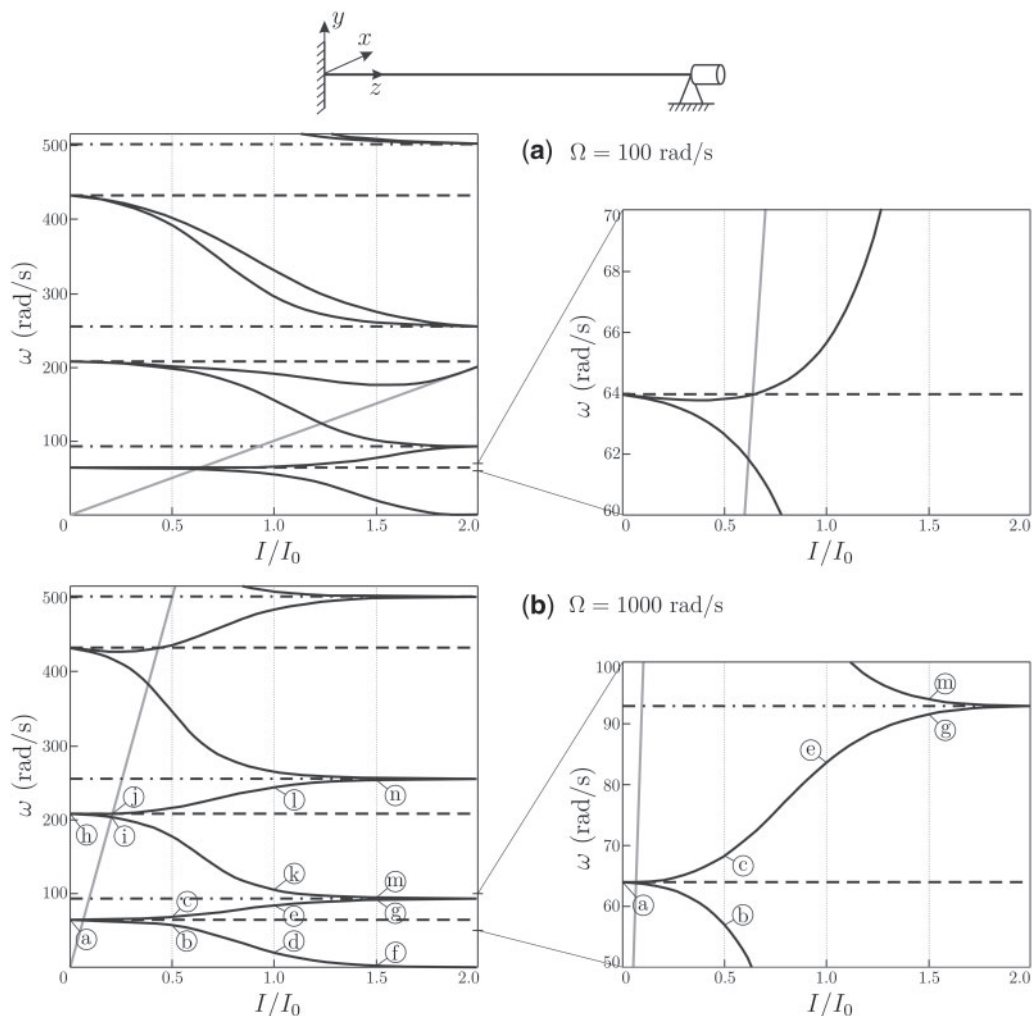
$$I = \frac{\pi \rho_{\text{gyr}}}{2} \gamma^4 \int_0^h f^4(\zeta) d\zeta, \quad I_0 = \frac{I}{2} + \pi \rho_{\text{gyr}} \gamma^2 \int_0^h \zeta^2 f^2(\zeta) d\zeta, \quad (5.3)$$

where  $\rho_{\text{gyr}}$  is the density of the spinner. The ratio  $I/I_0$  is then given by

$$\frac{I}{I_0} = \frac{2\gamma^2 \int_0^h f^4(\zeta) d\zeta}{\gamma^2 \int_0^h f^4(\zeta) d\zeta + 4 \int_0^h \zeta^2 f^2(\zeta) d\zeta}. \quad (5.4)$$

For fixed  $h$ , we observe that  $I/I_0 \rightarrow 0$  as  $\gamma \rightarrow 0$ , and  $I/I_0 \rightarrow 2$  as  $\gamma \rightarrow \infty$ .

In the following computations, we consider a cylindrical spinner with fixed height ( $h_{\text{cyl}} = 0.3$  m) and variable radius ( $0 \leq r_{\text{cyl}} < \infty$ ). A steel beam is considered ( $E = 210$  GPa,  $\rho = \rho_{\text{cyl}} = 7850$  kg/m<sup>3</sup>) with a square cross-section of side 0.1 m and length  $l = 6$  m.



**Fig. 4** Eigenfrequencies  $\omega$  of a beam with a clamped end and a gyro-hinged end as functions of the ratio  $I/I_0$ , calculated for two different values of the gyricity  $\Omega$ : (a)  $\Omega = 100 \text{ rad/s}$ , (b)  $\Omega = 1000 \text{ rad/s}$ . The gyroscopic spinner has a cylindrical shape. On the right, magnified insets of the dispersion diagrams are shown. The horizontal dashed and dot-dashed lines indicate the eigenfrequencies of a clamped-hinged beam and of a clamped-clamped beam, respectively, while the grey lines are defined by the equation  $\omega = I/I_0 \Omega$

### 5.1 Cylindrical gyroscopic spinner: beam with a clamped end and a gyro-hinge

We start by considering the case of a beam with a clamped end and a gyro-hinge, which was analysed in section 4.1 for a generic shape of the spinner.

The solid black lines in Fig. 4 are the eigenfrequencies of the beam shown as functions of the ratio  $I/I_0$ , calculated for two different values of the gyricity  $\Omega$  of the spinner. The horizontal dashed lines

represent the eigenfrequencies of the beam with a clamped end and a classical hinge, given by (4.5), while the horizontal dot-dashed lines are the eigenfrequencies of a beam with both ends clamped, obtained from (4.7). The inclined grey line is given by  $\omega = I/I_0 \Omega$ , which is the case of degeneracy discussed in section 3.1.

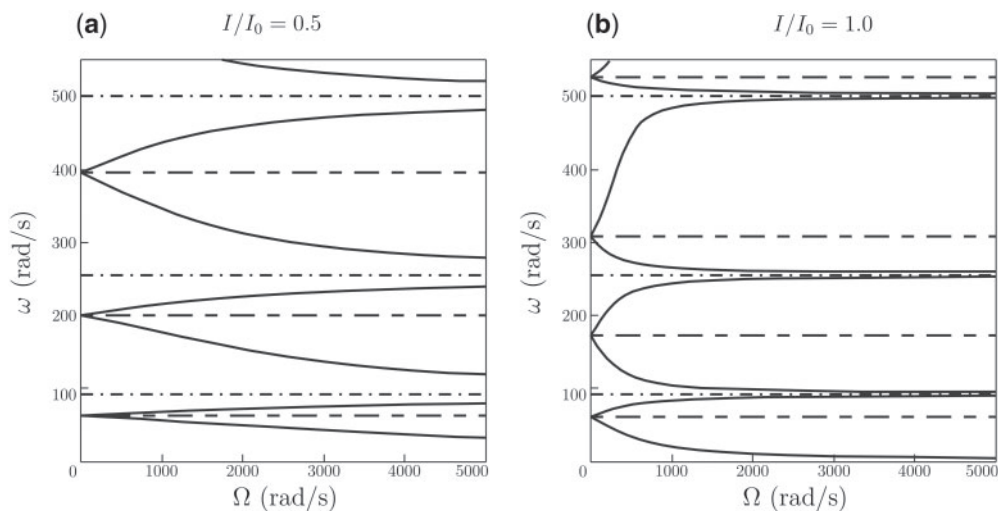
The following limiting cases deserve special attention:

- The case  $I/I_0 = 0$  corresponds to the situation when the gyroscopic spinner is removed from the right end of the beam and the gyro-hinge becomes a classical hinge. Indeed, in this case the eigenfrequencies of the beam have multiplicity 2 and they are equal to the eigenfrequencies of a clamped-hinged beam.
- For  $I/I_0 > 0$ , each pair of eigenfrequencies splits into two.
- When  $I/I_0 = \omega/\Omega$  (inclined grey lines), for each pair of eigenfrequencies, the smaller one coincides with the eigenfrequency of a clamped-hinged beam connected to a mass with rotational inertia  $2I_0$  at the hinged end, while the larger one is identical to the eigenfrequency of a clamped-hinged beam. Indeed, in the second case the inclined grey lines and the horizontal dashed lines intersect. We also note that for  $I/I_0 > \omega/\Omega$  one eigenfrequency is larger and the other one is smaller than the double eigenfrequency for  $I/I_0 = 0$ .
- When  $I/I_0 \rightarrow 2$ , the solid curves tend to the eigenfrequencies of a beam with both ends clamped. This result can be explained physically by recalling that, in this limit, the radius of the cylindrical spinner  $r_{\text{cyl}} \rightarrow \infty$ , hence the inertia of the spinner is so large that its axis does not change orientation. Accordingly, the axis of the beam does not vary its direction, simulating a clamped end.

In Fig. 5 we illustrate the dependance of the eigenfrequencies of the system on the gyricity  $\Omega$  for two fixed values of the ratio  $I/I_0$ . When  $\Omega = 0$ , the gyroscopic spinner behaves as a mass with rotational inertia  $I_0$ , and the corresponding double eigenfrequencies are obtained from (4.6). When  $\Omega > 0$  the eigenfrequencies split into two, one being smaller and one larger than the value for  $\Omega = 0$ . When  $\Omega \rightarrow \infty$ , the eigenfrequencies converge to the natural frequencies of a clamped-clamped beam, since in this case the gyricity of the system is so large that it does not allow for rotations at the hinged end of the beam.

**5.1.1 Eigenmodes.** The eigenmodes of the beam with clamped and gyro-hinged ends, determined for  $\Omega = 1000$  rad/s and corresponding to the eigenfrequencies indicated by the letters in Fig. 4b, are plotted in Fig. 6. In this figure, the red dots indicate the positions of the inflection points, namely the points where the bending moments are zero and the curvatures change sign. The eigenmodes denoted by ‘a’ and ‘h’ are identical to the first two eigenfunctions of a clamped-hinged beam. The eigenmodes determined for the same values of  $I/I_0 \neq 0$  and associated with the same vibration mode but characterised by different eigenfrequencies (such as modes ‘b’ and ‘c’, ‘d’ and ‘e’, etc.) have similar shape, but differ in the positions of the inflection points. For large values of  $I/I_0$ , the eigenmodes resemble the eigenfunctions of a clamped-clamped beam (see, for example, modes ‘g’, ‘m’ and ‘n’).

To better visualise the three-dimensional shapes of the eigenmodes in Fig. 6, we have computed the beam displacements  $u$  and  $v$ , given by (3.5), at different instants of time and for all the eigenfrequencies indicated by the letters in Fig. 4b. The motion of the beam for each eigenfrequency is displayed in the videos included in the Supplementary Material. When  $I/I_0 = 0$ , the beam does not rotate around its undeformed axis. Conversely, when  $I/I_0 \neq 0$ , the eigenmodes associated with



**Fig. 5** Eigenfrequencies  $\omega$  of a beam with a clamped end and a gyro-hinged end as functions of the gyrocity  $\Omega$  for (a)  $I/I_0 = 0.5$  and (b)  $I/I_0 = 1.0$ . The gyroscopic spinner has a cylindrical shape. The horizontal two-dashed lines indicate the eigenfrequencies of a clamped-hinged beam with a mass of rotational inertia  $I_0$  attached to the hinged end, while the dot-dashed lines are the eigenfrequencies of a clamped-clamped beam

eigenfrequencies belonging to the same curve rotate in the same direction (for instance, modes ‘b’, ‘d’ and ‘f’ rotate clockwise, while modes ‘c’, ‘e’ and ‘g’ rotate counter-clockwise).

The diagrams in Fig. 4 do not change if the spinner has the gyrocity of the same magnitude but of the opposite sign ( $\Omega < 0$ ). However, for each eigenfrequency in Fig. 4, the beam rotates in the opposite direction if the sign of  $\Omega$  is changed.

## 5.2 Cylindrical gyroscopic spinner: beam with a classical hinge and a gyro-hinge

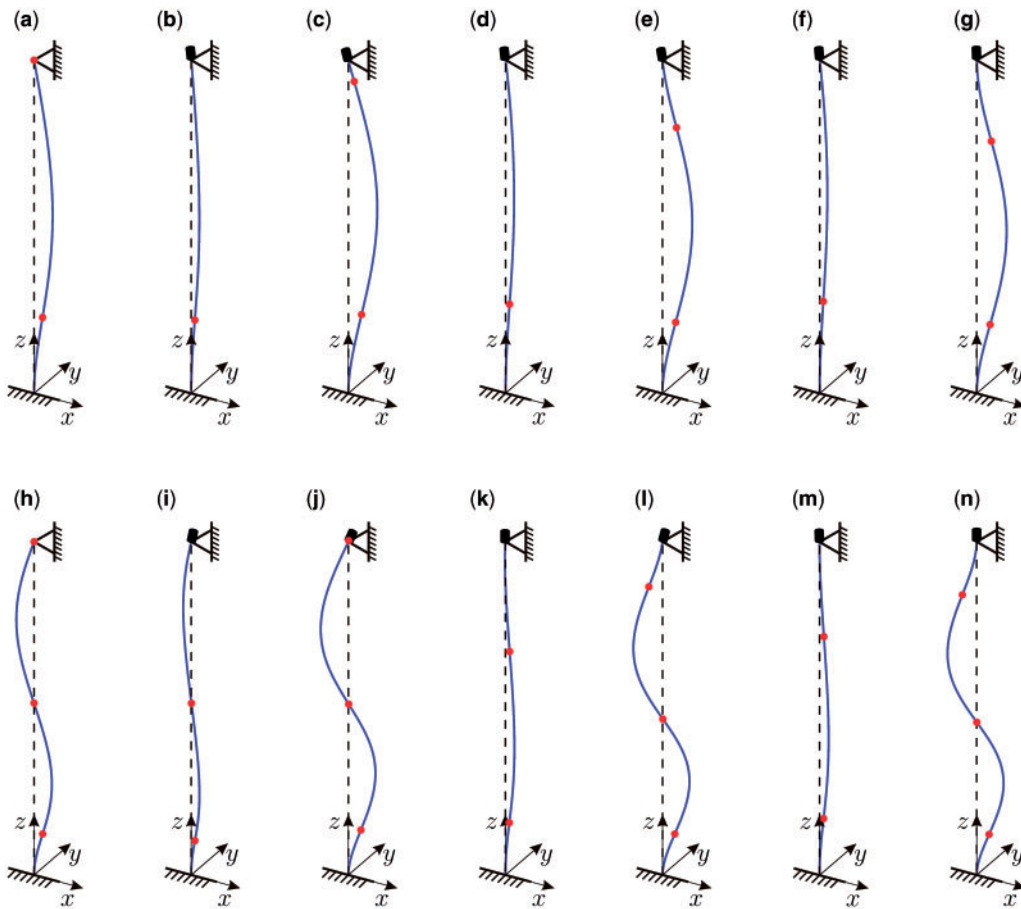
The analytical formulation used to determine the eigenfrequencies of a beam with a classical hinge and a gyro-hinge was presented in section 4.2 for a generic gyroscopic spinner.

When the spinner has a cylindrical shape, we show the eigenfrequencies  $\omega$  plotted in Fig. 7a as functions of the ratio  $I/I_0$ . The gyrocity is assumed to be  $\Omega = 1000$  rad/s. In the same figure, the horizontal dashed lines represent the eigenfrequencies of a clamped-hinged beam, derived from (4.5), while the horizontal dotted lines are the eigenfrequencies of a beam with classical hinges at the two ends, given by (see (36))

$$\sin^2(\beta l) = 0. \quad (5.5)$$

The power 2 in (5.5) indicates that the eigenfrequencies of a hinged-hinged beam with identical second moments of area in the principal directions have multiplicity 2.

The solid curves in Fig. 7a intersect the horizontal dotted lines at  $I/I_0 = 0$ , where the radius of the spinner vanishes. The same curves tend to the dashed lines in the limit when  $I/I_0 \rightarrow 2$ , where the inertia of the spinner attached to one end of the beam is so large that it does not precess. Hence, in this limit the gyro-hinge reacts as a clamped end, as discussed in section 5.1.



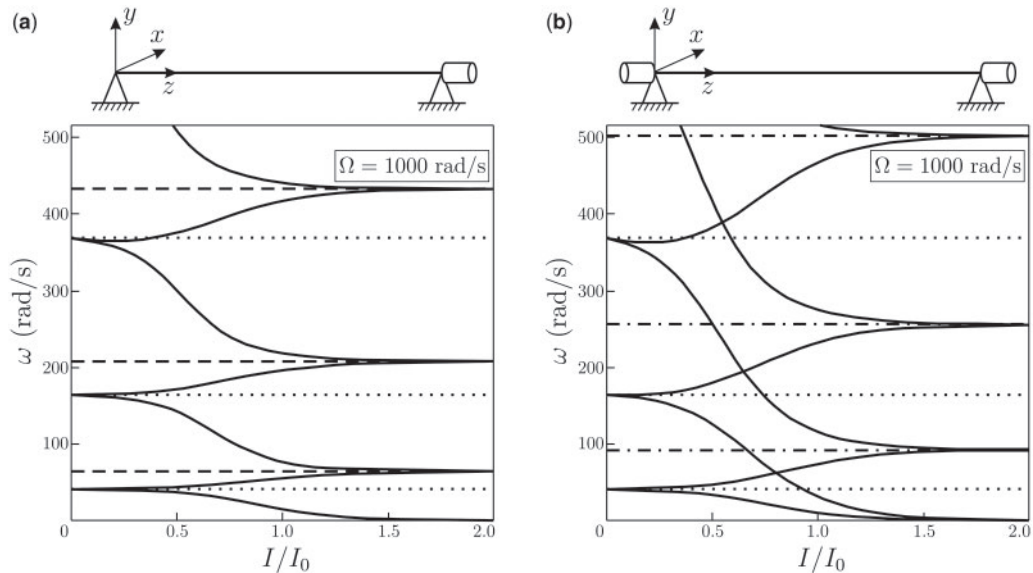
**Fig. 6** Eigenmodes of a beam with a clamped end and a gyro-hinged end, determined for  $\Omega = 1000$  rad/s and corresponding to the eigenfrequencies indicated by the small letters in Fig. 4b. The red dots represent the inflection points. In the cases 'a' and 'h', there is no gyroscopic spinner at  $z = l$

### 5.3 Cylindrical gyroscopic spinner: beam with two gyro-hinges

Figure 7b shows the eigenfrequencies of a beam with two gyro-hinges as functions of the ratio  $I/I_0$  of the cylindrical spinners attached at both ends. We note that in the computations the two spinners are identical. The eigenfrequencies are determined by using the formulation presented in section 4.3. The dotted and dot-dashed lines in Fig. 7b indicate the eigenfrequencies of a beam with two classical hinges and of a beam with two clamped ends, respectively.

With reference to Fig. 7b, it is interesting to notice that two eigenfrequencies of this beam tend to zero as  $I/I_0 \rightarrow 2$ . This is due to the fact that both ends of the beam are connected to gyroscopic spinners. The same observation would be expected for a beam with two rotational masses at its ends.

We also observe that, in this case, curves corresponding to different vibration modes intersect. Accordingly, eigenfunctions with different shapes are obtained at the same eigenfrequency.



**Fig. 7** Eigenfrequencies as function of  $I/I_0$  for (a) a beam with a hinged end and a gyro-hinged end, and (b) a beam with two gyro-hinged ends, both determined for  $\Omega = 1000$  rad/s. The gyroscopic spinner is a cylinder in both cases. The horizontal dotted, dashed and dot-dashed lines represent the eigenfrequencies of a hinged-hinged beam, of a hinged-clamped beam and of a clamped-clamped beam, respectively

## 6. Floquet–Bloch waves in a periodic structure of beams and gyro-hinges

In this section, we study a periodic structure consisting of continuous beams connected by gyro-hinges. The resulting dispersion relation will be used in section 7 to obtain an approximation for a periodic system of continuous gyrobeams connected by classical hinges.

The concept of a gyrobeam was proposed in (27), where the governing equations coupled displacement components perpendicular to the beam axis and a gyricity parameter was introduced representing a ‘continuous distribution of stored angular momentum’. In section 7.2, we provide an interpretation of the gyricity parameter in terms of geometrical and inertial parameters of the system.

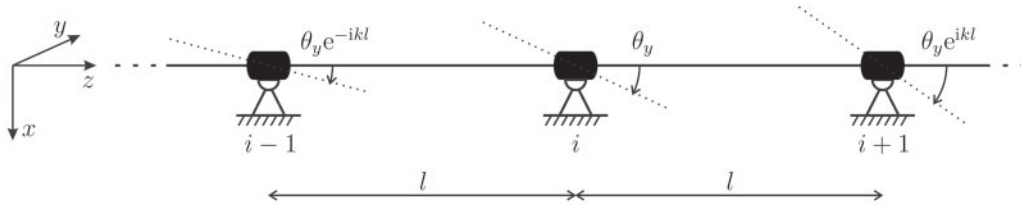
### 6.1 Derivation of the dispersion relation

We consider a periodic beam with gyro-hinges symbolically shown in Fig. 8. The distance between the supports is denoted by  $l$ .

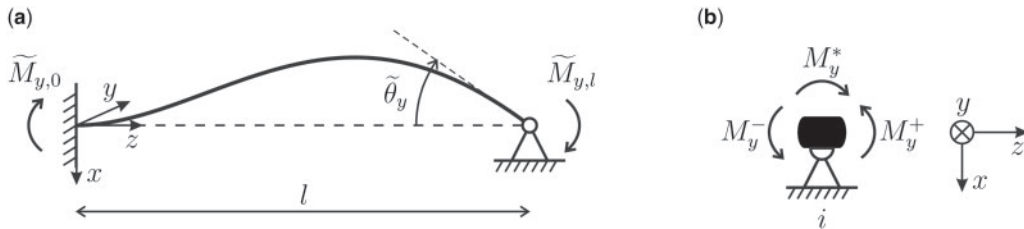
At the supports the displacements are zero, while the rotations are generally different from zero. We define  $\theta_y^i$  as the rotation about the  $y$ -axis at the  $i$ th junction. Since the structure is periodic, we can impose the Floquet–Bloch conditions (see (38, 39)), whereby the rotations around the  $y$ -axis at the  $(i - 1)$ th and  $(i + 1)$ th nodes are related to the rotation at the  $i$ th node as follows:

$$\theta_y^{i-1} = \theta_y^i e^{-ikl}, \quad \theta_y^{i+1} = \theta_y^i e^{ikl}, \quad (6.1)$$





**Fig. 8** Periodic beam with gyro-hinges at the junctions



**Fig. 9** Auxiliary diagrams used to derive the dispersion relation for the periodic beam in Fig. 8: (a) a finite beam clamped at the left end and with zero displacement and prescribed rotation  $\tilde{\theta}_y$  at the right end; (b) the balance of moments around the  $y$ -axis at the junction, where  $M_y^*$  is the bending moment around the  $y$ -axis induced by the gyroscopic spinner

where  $\theta_y = \theta_y^i$ . Similar conditions apply to the rotations around the  $x$ -axis. Here  $k$  is the wavenumber or Bloch parameter, which is inversely proportional to the wavelength  $\lambda = 2\pi/k$  (see (40)).

At the  $i$ th junction point, the bending moments of the beam ( $M_y^-$ , on the left, and  $M_y^+$ , on the right) need to balance the moment produced by the gyroscopic spinner ( $M_y^*$ ), as shown in Fig. 9b. By using the first of the time-harmonic gyro-hinge boundary conditions (3.6), we obtain the following expression for  $M_y^*$ :

$$M_y^* = I_0 \omega^2 \theta_y - i \omega I \Omega \theta_x. \tag{6.2}$$

The moments  $M_y^-$  and  $M_y^+$  can be determined by means of the Floquet–Bloch conditions and the superposition principle, whereby  $M_y^-$  ( $M_y^+$ ) is derived by summing the bending moments due to the rotations at the ends of the beam on the left (right) of the  $i$ th node. For this purpose, we study the simple Euler–Bernoulli beam in Fig. 9a, which is assumed to deform in the  $xz$ -plane. The beam has zero displacement and zero rotation at the left end ( $U = 0, \theta_y = 0$  at  $z = 0$ ) and zero displacement and unit rotation at the right end ( $U = 0, \theta_y = \tilde{\theta}_y = 1$  at  $z = l$ ). By using the general solution (4.2a) for the beam displacement component  $U$  and the boundary conditions indicated above, the corresponding bending moments at the left and right ends can be written as (see also (41, 42))

$$\tilde{M}_{y,0} = \frac{EJ\beta [\sinh(\beta l) - \sin(\beta l)]}{1 - \cos(\beta l) \cosh(\beta l)}, \tag{6.3a}$$

$$\tilde{M}_{y,l} = \frac{EJ\beta [\sin(\beta l) \cosh(\beta l) - \cos(\beta l) \sinh(\beta l)]}{1 - \cos(\beta l) \cosh(\beta l)}. \tag{6.3b}$$

By employing the Floquet–Bloch conditions (6.1), the moments on the left and on the right of the  $i$ th node are given by (see Figs. 8 and 9b)

$$M_y^- = \tilde{M}_{y,l} \theta_y + \tilde{M}_{y,0} \theta_y e^{-ikl}, \quad (6.4a)$$

$$M_y^+ = \tilde{M}_{y,l} \theta_y + \tilde{M}_{y,0} \theta_y e^{ikl}. \quad (6.4b)$$

Equations (6.2) and (6.4) are then substituted into the equation of balance of moments  $M_y^- + M_y^+ - M_y^* = 0$  (see Fig. 9b). By following the same procedure for the moments around the  $x$ -axis, we derive the following system of equations written in matrix form:

$$\begin{pmatrix} 2\tilde{M}_{y,l} + 2\tilde{M}_{y,0} \cos(kl) - I_0\omega^2 & -i\omega I\Omega \\ i\omega I\Omega & 2\tilde{M}_{y,l} + 2\tilde{M}_{y,0} \cos(kl) - I_0\omega^2 \end{pmatrix} \begin{pmatrix} \theta_x \\ \theta_y \end{pmatrix} = \begin{pmatrix} 0 \\ 0 \end{pmatrix}. \quad (6.5)$$

The non-trivial solution of (6.5) exists if

$$\left[ 2\tilde{M}_{y,l} + 2\tilde{M}_{y,0} \cos(kl) - I_0\omega^2 \right]^2 - \omega^2 I^2 \Omega^2 = 0, \quad (6.6)$$

which represents the dispersion relation of the periodic beam with gyro-hinges. When the spinners are removed from the system, (6.6) reduces to the classical dispersion relation of a periodically simply-supported beam (41, 42):

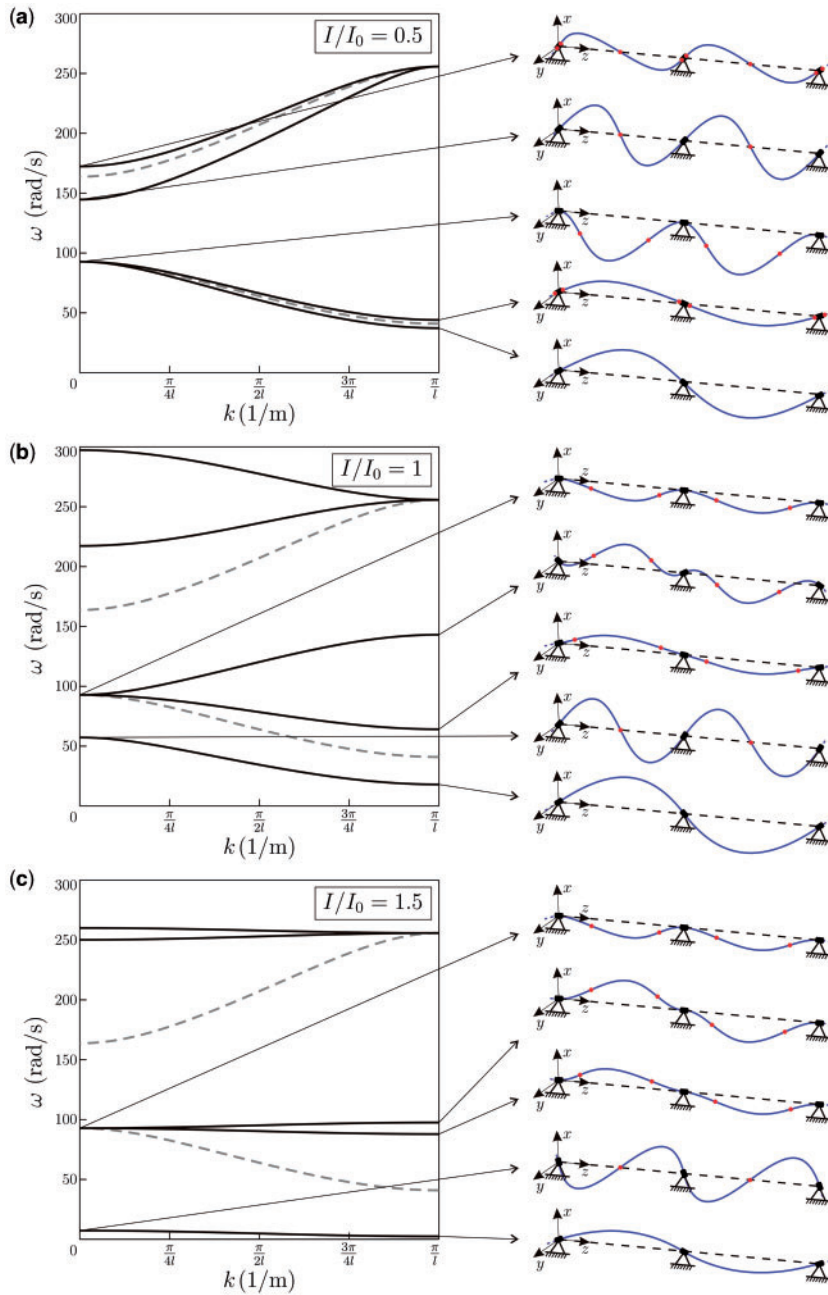
$$\left[ 2\tilde{M}_{y,l} + 2\tilde{M}_{y,0} \cos(kl) \right]^2 = 0. \quad (6.7)$$

## 6.2 Dispersion diagrams

The dispersion curves derived from the relation (6.6) for the periodic system of beams on gyro-hinges are plotted as solid lines in Fig. 10 for three values of the ratio  $I/I_0$  and for a spin rate equal to  $\Omega = 1000$  rad/s. This value of  $\Omega$  was chosen because it allows a clear description of the effect of the gyroscopes on the dynamic behaviour of the beam. The values of the other quantities are the same as those specified in section 5. The dashed lines in the same figure are the dispersion curves for a beam, simply-supported on periodically-spaced supports, obtained from (6.7).

The dashed lines represent double roots of the dispersion equation (6.7), since the second moments of area of the beam cross-section with respect to the  $x$ - and  $y$ -axis are taken here identical. In this case, flexural waves in the two directions  $x$  and  $y$  are not coupled. When gyroscopic spinners are attached to the beam at the supports, the dispersion equation does not have double roots for  $0 < k < \pi$ .

Figure 10a corresponds to the case  $I/I_0 = 0.5$ . In this figure, each of the dashed curves is split into two solid curves. For the lowest two vibration modes of the structure shown in Fig. 10a, one dispersion curve is lower and one is higher than the dashed dispersion curve corresponding to a periodically simply-supported beam without spinners. This observation is in line with the eigenfrequency analysis of a finite beam with a gyro-hinge, as shown in Fig. 4c for  $I/I_0 = 0.5$ , where for the first two vibration modes one eigenfrequency is smaller and one is larger than the double eigenfrequency of a beam without spinners. The eigenmodes are illustrated in the right part of Fig. 10a. Although neighbouring eigenmodes are similar in shape, they differ in the number and positions of inflection points, represented by the red dots, and in the direction of rotation about  $z$ -axis. The eigenmodes



**Fig. 10** Dispersion curves for a periodic system of beams supported by gyro-hinges, calculated for  $\Omega = 1000$  rad/s and for (a)  $I/I_0 = 0.5$ , (b)  $I/I_0 = 1.0$ , (c)  $I/I_0 = 1.5$ . The dashed lines represent the dispersion curves for a periodically simply-supported beam. On the right, some instances of eigenfunctions are shown, where the red dots indicate the inflection points

determined at the frequencies where two dispersion curves intersect (both at  $k = 0$  and  $k = \pi/l$ ) resemble the eigenfunctions of a beam with clamped ends. Indeed, these frequencies coincide with the eigenfrequencies of a finite beam with two clamped ends (see Fig. 4c).

When  $I/I_0 = 1$  (see Fig. 10b), one dispersion curve occurs at lower frequencies, while the other dispersion curves appear in pairs and at higher frequencies than those corresponding to dispersion curves for a periodic beam without spinners. As the ratio  $I/I_0$  is increased, the low dispersion curve moves to smaller frequencies, while the higher dispersion curves tend to become closer to each other in pairs. This is shown for the case  $I/I_0 = 1.5$  in Fig. 10c. Additionally for this case, the dispersion analysis presents similarities with the eigenfrequency study of a finite beam. As shown in Fig. 4c, when  $I/I_0 \rightarrow 2$  one eigenfrequency is very small and the others tend to the natural frequencies of a clamped-clamped beam. Indeed, the eigenmodes associated with the dispersion curves at higher frequencies resemble the eigenfunctions of beams with clamped ends.

The results presented in Fig. 10 show that the size and position of each band-gap can be varied by changing the properties of the spinners. In addition, some limits of the band-gaps can be predicted by solving problems for finite beams with appropriate boundary conditions at the ends.

## 7. Comparison between a gyrobeam and a beam with gyro-hinges

A gyrobeam is a theoretical structural element, representing an Euler–Bernoulli beam with a continuous distribution of stored angular momentum. Initially introduced in (27), it was recently used as a tunable resonator for seismic applications in (33). In this section, we show that a periodic simply-supported gyrobeam can be dynamically approximated by a periodic beam on gyro-hinges in the time-harmonic regime.

### 7.1 Dispersion relation for a periodic simply-supported gyrobeam

In the time-harmonic regime, the equations of motion for a gyrobeam are expressed by (27, 33)

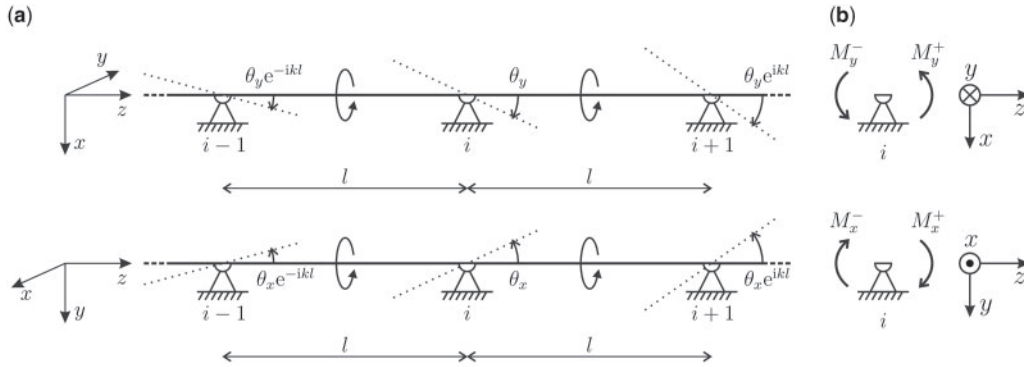
$$EJ \frac{d^4 U}{dz^4} - \rho \mathcal{A} \omega^2 U + ih\omega \frac{d^2 V}{dz^2} = 0, \quad (7.1a)$$

$$EJ \frac{d^4 V}{dz^4} - \rho \mathcal{A} \omega^2 V - ih\omega \frac{d^2 U}{dz^2} = 0. \quad (7.1b)$$

As in section 3,  $U = U(z)$  and  $V = V(z)$  denote the amplitudes of the displacement components in the  $x$  and  $y$  directions respectively, and  $z$  is the direction of the gyrobeam axis. Here  $h$  is the *gyricity constant*, which is a theoretical parameter introduced in (27) that we will interpret in terms of geometrical and inertial parameters of the system. The other parameters in (7.1) have the same meaning as in section 2.2. The general solutions of (7.1) are given by

$$U(z) = A_1 \cos(\beta_+ z) + A_2 \sin(\beta_+ z) + A_3 \cosh(\beta_+ z) + A_4 \sinh(\beta_+ z) \\ + A_5 \cos(\beta_- z) + A_6 \sin(\beta_- z) + A_7 \cosh(\beta_- z) + A_8 \sinh(\beta_- z), \quad (7.2a)$$

$$V(z) = i[A_1 \cos(\beta_+ z) + A_2 \sin(\beta_+ z) - A_3 \cosh(\beta_+ z) - A_4 \sinh(\beta_+ z) \\ - A_5 \cos(\beta_- z) - A_6 \sin(\beta_- z) + A_7 \cosh(\beta_- z) + A_8 \sinh(\beta_- z)], \quad (7.2b)$$



**Fig. 11** (a) Infinite gyrobeam on periodically-spaced supports; (b) moments at the generic  $i$ th node. Two different views are presented to show the rotations and the moments of the system in different planes

where  $A_i$  ( $1 \leq i \leq 8$ ) are arbitrary constants and

$$\beta_{\pm} = \sqrt{\frac{\omega \left[ \mp h + \sqrt{h^2 + 4EJ\rho\mathcal{A}} \right]}{2EJ}}. \quad (7.3)$$

As in section 6.1, we use the superposition principle and the Floquet–Bloch conditions to derive the dispersion relation for an infinite gyrobeam resting on periodically-spaced supports. We consider the periodic gyrobeam in Fig. 11a, shown from two different viewpoints. The bending moments acting on the generic  $i$ th node are denoted as  $M_y^-$ ,  $M_y^+$ ,  $M_x^-$  and  $M_x^+$  in Fig. 11b. These moments can be determined by employing the Floquet–Bloch conditions as follows:

$$M_y^- = \tilde{M}_{y,l}^{(a)}\theta_y + \tilde{M}_{y,l}^{(b)}\theta_y e^{-ikl} + \tilde{M}_{y,l}^{(c)}\theta_x + \tilde{M}_{y,l}^{(d)}\theta_x e^{-ikl}, \quad (7.4a)$$

$$M_y^+ = \tilde{M}_{y,0}^{(b)}\theta_y + \tilde{M}_{y,0}^{(a)}\theta_y e^{ikl} + \tilde{M}_{y,0}^{(d)}\theta_x + \tilde{M}_{y,0}^{(c)}\theta_x e^{ikl}, \quad (7.4b)$$

$$M_x^- = \tilde{M}_{x,l}^{(a)}\theta_y + \tilde{M}_{x,l}^{(b)}\theta_y e^{-ikl} + \tilde{M}_{x,l}^{(c)}\theta_x + \tilde{M}_{x,l}^{(d)}\theta_x e^{-ikl}, \quad (7.4c)$$

$$M_x^+ = \tilde{M}_{x,0}^{(b)}\theta_y + \tilde{M}_{x,0}^{(a)}\theta_y e^{ikl} + \tilde{M}_{x,0}^{(d)}\theta_x + \tilde{M}_{x,0}^{(c)}\theta_x e^{ikl}, \quad (7.4d)$$

where  $\theta_y$  is the rotation of the gyrobeam at the  $i$ th node around the  $y$ -axis (see Fig. 11a). The quantities with tildes in (7.4) are the bending moments acting at the ends of the beams shown in Figs. 12a–12d.

For example, the beam in Fig. 12a has the following boundary conditions:

$$U^{(a)}\Big|_{z=0} = 0, \quad U'^{(a)}\Big|_{z=0} = 0, \quad V^{(a)}\Big|_{z=0} = 0, \quad V'^{(a)}\Big|_{z=0} = 0, \quad (7.5a)$$

$$U^{(a)}\Big|_{z=l} = 0, \quad U'^{(a)}\Big|_{z=l} = \tilde{\theta}_y^{(a)} = 1, \quad V^{(a)}\Big|_{z=l} = 0, \quad V'^{(a)}\Big|_{z=l} = 0, \quad (7.5b)$$

where prime denotes derivative with respect to  $z$ . The coefficients  $A_i$  ( $1 \leq i \leq 8$ ) of the displacement components  $U$  and  $V$  are found by substituting the general solutions (7.2) into the boundary

conditions (7.5) and solving the resulting system of algebraic equations. The bending moments at the ends of the beam are given by the following:

$$\begin{aligned} \tilde{M}_{y,l}^{(a)} = EJ U''^{(a)} \Big|_{z=l} &= -EJ \{[(\cos(\beta_+l) - \cosh(\beta_-l)) \\ &\times (\beta_-^2 \beta_+ \sinh(\beta_-l) + \beta_- \beta_+^2 \sin(\beta_+l)) + (\beta_+^2 \cos(\beta_+l) + \beta_-^2 \cosh(\beta_-l)) \\ &\times (\beta_+ \sinh(\beta_-l) - \beta_- \sin(\beta_+l))] / D_1 + [(\cos(\beta_-l) - \cosh(\beta_+l)) \\ &\times (\beta_+^2 \beta_- \sinh(\beta_+l) + \beta_+ \beta_-^2 \sin(\beta_-l)) + (\beta_-^2 \cos(\beta_-l) + \beta_+^2 \cosh(\beta_+l)) \\ &\times (\beta_- \sinh(\beta_+l) - \beta_+ \sin(\beta_-l))] / D_2\}, \end{aligned} \quad (7.6a)$$

$$\begin{aligned} \tilde{M}_{y,0}^{(a)} = -EJ U''^{(a)} \Big|_{z=0} &= EJ (\beta_+^2 + \beta_-^2) \{[\beta_+ \sinh(\beta_-l) - \beta_- \sin(\beta_+l)] / D_1 \\ &+ [\beta_- \sinh(\beta_+l) - \beta_+ \sin(\beta_-l)] / D_2\}, \end{aligned} \quad (7.6b)$$

$$\begin{aligned} \tilde{M}_{x,l}^{(a)} = -EJ V''^{(a)} \Big|_{z=l} &= iEJ \{[(\cos(\beta_+l) - \cosh(\beta_-l)) \\ &\times (\beta_-^2 \beta_+ \sinh(\beta_-l) + \beta_- \beta_+^2 \sin(\beta_+l)) + (\beta_+^2 \cos(\beta_+l) + \beta_-^2 \cosh(\beta_-l)) \\ &\times (\beta_+ \sinh(\beta_-l) - \beta_- \sin(\beta_+l))] / D_1 - [(\cos(\beta_-l) - \cosh(\beta_+l)) \\ &\times (\beta_+^2 \beta_- \sinh(\beta_+l) + \beta_+ \beta_-^2 \sin(\beta_-l)) + (\beta_-^2 \cos(\beta_-l) + \beta_+^2 \cosh(\beta_+l)) \\ &\times (\beta_- \sinh(\beta_+l) - \beta_+ \sin(\beta_-l))] / D_2\}, \end{aligned} \quad (7.6c)$$

$$\begin{aligned} \tilde{M}_{x,0}^{(a)} = EJ V''^{(a)} \Big|_{z=0} &= -iEJ (\beta_+^2 + \beta_-^2) \{[\beta_+ \sinh(\beta_-l) - \beta_- \sin(\beta_+l)] / D_1 \\ &- [\beta_- \sinh(\beta_+l) - \beta_+ \sin(\beta_-l)] / D_2\}, \end{aligned} \quad (7.6d)$$

where

$$D_1 = 4\beta_+\beta_- (1 - \cos(\beta_+l) \cosh(\beta_-l)) - 2(\beta_+^2 - \beta_-^2) \sin(\beta_+l) \sinh(\beta_-l), \quad (7.7a)$$

$$D_2 = 4\beta_-\beta_+ (1 - \cos(\beta_-l) \cosh(\beta_+l)) - 2(\beta_-^2 - \beta_+^2) \sin(\beta_-l) \sinh(\beta_+l). \quad (7.7b)$$

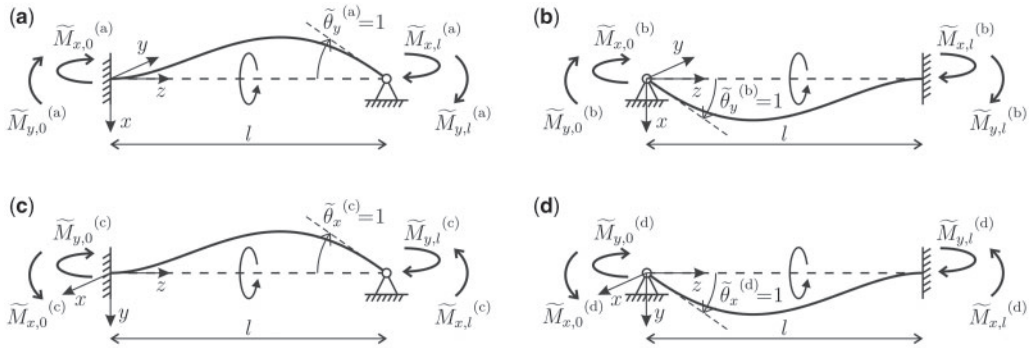
Following a similar procedure, the bending moments at the ends of the beams displayed in Figs. 12b–d are given by

$$\tilde{M}_{y,l}^{(b)} = \tilde{M}_{y,0}^{(a)}, \quad \tilde{M}_{y,0}^{(b)} = \tilde{M}_{y,l}^{(a)}, \quad \tilde{M}_{x,l}^{(b)} = \tilde{M}_{x,0}^{(a)}, \quad \tilde{M}_{x,0}^{(b)} = \tilde{M}_{x,l}^{(a)}, \quad (7.8a)$$

$$\tilde{M}_{y,l}^{(c)} = \tilde{M}_{x,l}^{(a)}, \quad \tilde{M}_{y,0}^{(c)} = \tilde{M}_{x,0}^{(a)}, \quad \tilde{M}_{x,l}^{(c)} = -\tilde{M}_{y,l}^{(a)}, \quad \tilde{M}_{x,0}^{(c)} = -\tilde{M}_{y,0}^{(a)}, \quad (7.8b)$$

$$\tilde{M}_{y,l}^{(d)} = \tilde{M}_{x,0}^{(a)}, \quad \tilde{M}_{y,0}^{(d)} = \tilde{M}_{x,l}^{(a)}, \quad \tilde{M}_{x,l}^{(d)} = -\tilde{M}_{y,0}^{(a)}, \quad \tilde{M}_{x,0}^{(d)} = -\tilde{M}_{y,l}^{(a)}, \quad (7.8c)$$

respectively.



**Fig. 12** Finite gyrobeams with different boundary conditions, used in the derivation of the dispersion relation for the periodic structure in Fig. 11: (a) clamped end at  $z = 0$  and classical hinge with prescribed rotation  $\tilde{\theta}_y = 1$  at  $z = l$ ; (b) classical hinge with prescribed rotation  $\tilde{\theta}_y = 1$  at  $z = 0$  and clamped end at  $z = l$ ; (c) clamped end at  $z = 0$  and classical hinge with prescribed rotation  $\tilde{\theta}_x = 1$  at  $z = l$ ; (d) classical hinge with prescribed rotation  $\tilde{\theta}_x = 1$  at  $z = 0$  and clamped end at  $z = l$

The equations of balance of moments at the  $i$ th node are given by  $M_y^- + M_y^+ = 0$  and  $M_x^- + M_x^+ = 0$  (see Fig. 11b). They can be re-written in the following matrix form by using (7.4) and (7.8):

$$\begin{pmatrix} \tilde{M}_{x,l}^{(a)} + \tilde{M}_{x,0}^{(a)} \cos(kl) & \tilde{M}_{y,l}^{(a)} + \tilde{M}_{y,0}^{(a)} \cos(kl) \\ -(\tilde{M}_{y,l}^{(a)} + \tilde{M}_{y,0}^{(a)} \cos(kl)) & \tilde{M}_{x,l}^{(a)} + \tilde{M}_{x,0}^{(a)} \cos(kl) \end{pmatrix} \begin{pmatrix} \theta_x \\ \theta_y \end{pmatrix} = \begin{pmatrix} 0 \\ 0 \end{pmatrix}. \quad (7.9)$$

The non-trivial solution of (7.9) exists if

$$\left[ \tilde{M}_{x,l}^{(a)} + \tilde{M}_{x,0}^{(a)} \cos(kl) \right]^2 + \left[ \tilde{M}_{y,l}^{(a)} + \tilde{M}_{y,0}^{(a)} \cos(kl) \right]^2 = 0 \quad (7.10)$$

or, equivalently, if

$$\left| \frac{\tilde{M}_{x,l}^{(a)} + \tilde{M}_{x,0}^{(a)} \cos(kl)}{\tilde{M}_{y,l}^{(a)} + \tilde{M}_{y,0}^{(a)} \cos(kl)} \right| = 1, \quad (7.11)$$

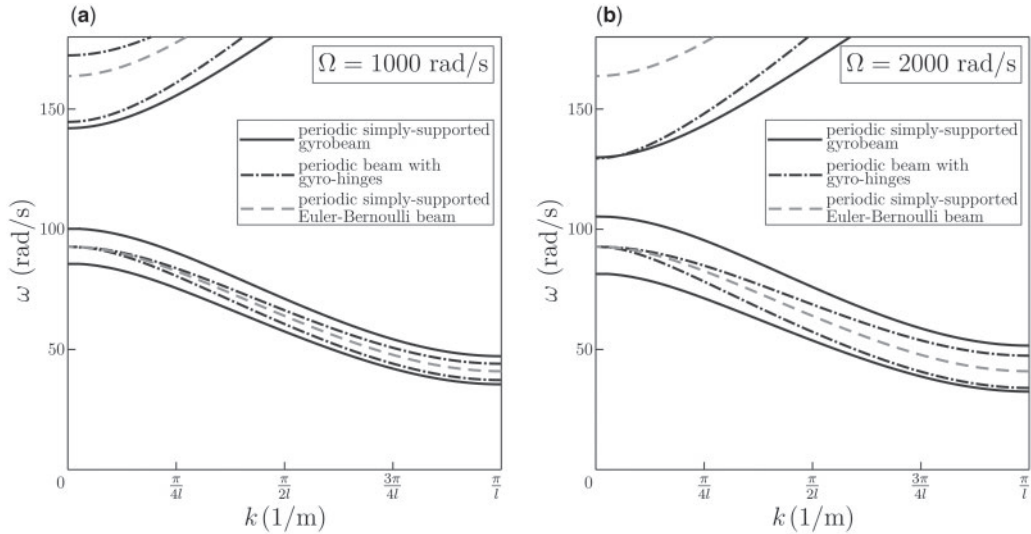
where the quantities  $\tilde{M}_{x,l}^{(a)}$ ,  $\tilde{M}_{x,0}^{(a)}$ ,  $\tilde{M}_{y,l}^{(a)}$  and  $\tilde{M}_{y,0}^{(a)}$  are given by (7.6).

### 7.2 Interpretation of the gyricity constant of a gyrobeam

In this section, we show that at sufficiently low frequencies in the time-harmonic regime we can approximate a gyrobeam on periodically-spaced supports by a periodic beam with gyro-hinges.

We take  $k = \pi/l$ , corresponding to the boundary of the irreducible Brillouin zone. The Taylor expansions computed up to the second term in  $\omega^2$  in the left-hand sides of the dispersion relations (6.6) and (7.10) then give

$$\frac{4(EJ)^2}{l^2} - \frac{[4EJ(\rho \mathcal{A} l^3 + 30I_0) + 15lI^2\Omega^2]\omega^2}{60l} \quad (7.12)$$



**Fig. 13** Dispersion curves for a periodic simply-supported gyrobeam (solid lines), for a periodic beam with gyro-hinges (dot-dashed lines) and for a periodic simply-supported Euler–Bernoulli beam (dashed lines). The dot-dashed curves are determined for  $I/I_0 = 0.5$  and for (a)  $\Omega = 1000$  rad/s, (b)  $\Omega = 2000$  rad/s. The values of the gyricity constant  $h$  used to calculate the dispersion curves for the periodic simply-supported gyrobeam (solid lines), obtained from Eq. (7.14), are the following: (a)  $h = 3344.8$  Ns, (b)  $h = 5473.1$  Ns

and

$$\frac{4(EJ)^2}{l^2} - \frac{[(12EJ\rho A + 7h^2)l^2]\omega^2}{180}, \quad (7.13)$$

respectively. The expressions (7.12) and (7.13) are equal if

$$h = \pm 3\sqrt{\frac{5(8EJ I_0 + lI^2\Omega^2)}{7l^3}}. \quad (7.14)$$

The gyricity constant  $h$  depends on the parameters of the spinner ( $I$ ,  $I_0$  and  $\Omega$ , and hence  $\dot{\phi}$  and  $\dot{\psi}$  through (3.3)) as well as on the length  $l$  and the flexural stiffness  $EJ$  of the beam. We point out that the approximation (7.14) always leads to real values of  $h$ .

In Fig. 13, the dot-dashed lines represent the dispersion curves for a periodic beam on gyro-hinges, calculated for  $I/I_0 = 0.5$  and for  $\Omega = 1000$  rad/s (part a) and  $\Omega = 2000$  rad/s (part b). The solid lines are the dispersion curves for a periodic simply-supported gyrobeam, where  $h$  is determined from (7.14). In the same figure, the dispersion curves for a periodic simply-supported Euler–Bernoulli beam are shown by dashed lines for comparison.

From Fig. 13 it is apparent that the low-frequency dynamic behaviour of a gyrobeam on periodically-spaced supports can be well described by a periodic distribution of Euler–Bernoulli beams connected by gyro-hinges. Of course, the approximation is more accurate for large values of the wavenumber, because the Taylor expansions were determined at  $k = \pi/l$ .



We emphasise that the low-frequency behaviour of a gyrobeam is very important for seismic applications since, in the low-frequency regime, gyrobeams can be used as an efficient tool to absorb vibrations of a multi-scale structure subjected to seismic loads (33).

## 8. Conclusions

Three classes of new results have been obtained in this article.

First, we have provided an interpretation of a gyrobeam. The latter existed in the literature as a mathematical model (27). The periodic chiral system proposed in the present article provides an asymptotic approximation of a gyrobeam, which includes an expression for the gyricity coefficient of a gyrobeam in terms of geometrical and inertial parameters of the system (refer to (7.14)).

Secondly, a new type of a chiral multi-structure has been introduced and studied, by combining an elastic Euler–Bernoulli beam and a gyroscopic spinner. Asymptotic analysis has led to a new type of chiral boundary condition, referred to as the ‘gyro-hinge boundary condition’. The corresponding eigenvalue problems have been analysed and eigensolutions, which represent coupled flexural modes of different polarisations, have been obtained. It has been shown that the eigenfrequencies and eigenmodes of a beam with gyro-hinges can be tuned by modifying the properties of the spinner, in particular its moments of inertia ( $I$  and  $I_0$ ) and gyricity ( $\Omega$ ), as demonstrated for example in Figs. 4, 5 and 6. For the convenience of the reader, the table in Fig. 2 is provided to summarise the analytical expressions for the natural frequencies of beams with chiral boundary conditions.

Finally, Floquet–Bloch waves have been studied in a periodic flexural system, embedding gyro-hinge junction conditions. The dispersion relation for a periodic beam on gyro-hinges has been derived in a closed analytical form. We have discussed how the resulting dispersion curves are affected by the rotational motion of the spinners. In particular, we have shown how the width and position of band-gaps can be varied by changing the parameters of the spinners (see Fig. 10).

## Acknowledgement

The authors would like to thank the EPSRC (UK) for its support through Programme Grant no. EP/L024926/1. M.J.N. gratefully acknowledges the support of the EU H2020 grant MSCA-IF-2016-747334-CAT-FFLAP.

## Supplementary data

Supplementary data (videos) are available online at *Quarterly Journal of Mechanics and Applied Mathematics*.

## References

1. W. Thomson, *The Molecular Tactics of a Crystal*, 1st edn., (Clarendon Press, Oxford 1894).
2. D. Prall and R. S. Lakes, Properties of a chiral honeycomb with a Poisson’s ratio of -1, *Int. J. Mech. Sci.* **39** (1997) 305–314.
3. A. Spadoni and M. Ruzzene, Elasto-static micropolar behavior of a chiral auxetic lattice, *J. Mech. Phys. Solids* **60** (2012) 156–171.
4. A. Spadoni, M. Ruzzene, S. Gonella and F. Scarpa, Phononic properties of hexagonal chiral lattices, *Wave Motion* **46** (2009) 435–450.

5. K. F. Tee, A. Spadoni, F. Scarpa and M. Ruzzene, Wave propagation in auxetic tetrachiral honeycombs, *J. Vib. Acoust.* **132** (2010) 031007.
6. D. Bigoni, S. Guenneau, A. B. Movchan and M. Brun, Elastic metamaterials with inertial locally resonant structures: application to lensing and localization, *Phys. Rev. B* **87** (2013) 174343.
7. R. Zhu, X. N. Liu, G. K. Hu, C. T. Sun and G. L. Huang, A chiral elastic metamaterial beam for broadband vibration suppression, *J. Sound Vib.* **333** (2014) 2759–2773.
8. D. Tallarico, N. V. Movchan, A. B. Movchan and D. J. Colquitt, Tilted resonators in a triangular elastic lattice: chirality, Bloch waves and negative refraction, *J. Mech. Phys. Solids* **103** (2017) 236–256.
9. D. Tallarico, A. Trevisan, N. V. Movchan and A. B. Movchan, Edge waves and localization in lattices containing tilted resonators, *Front. Mater.* **4** (2017) 16.
10. M. Brun, I. S. Jones and A. B. Movchan, Vortex-type elastic structured media and dynamic shielding, *Proc. R. Soc. A* **468** (2012) 3027–3046.
11. G. Carta, M. Brun, A. B. Movchan, N. V. Movchan and I. S. Jones, Dispersion properties of vortex-type monatomic lattices, *Int. J. Solids Struct.* **51** (2014) 2213–2225.
12. L. M. Nash, D. Kleckner, A. Read, V. Vitelli, A. M. Turner and W. T. M. Irvine, Topological mechanics of gyroscopic metamaterials, *Proc. Natl. Acad. Sci.* **112** (2015) 14495–14500.
13. P. Wang, L. Lu and K. Bertoldi, Topological phononic crystals with one-way elastic edge waves, *Phys. Rev. Lett.* **115** (2015) 104302.
14. G. Carta, I. S. Jones, N. V. Movchan, A. B. Movchan and M. J. Nieves, ‘Deflecting elastic prism’ and unidirectional localisation for waves in chiral elastic systems, *Sci. Rep.* **7** (2017) 26.
15. D. J. Mead, Free wave propagation in periodically supported, infinite beams, *J. Sound Vib.* **11** (1970) 181–197.
16. G. Sen Gupta, Natural flexural waves and the normal modes of periodically-supported beams and plates, *J. Sound Vib.* **13** (1970) 89–101.
17. D. J. Mead, Wave propagation and natural modes in periodic systems: II. Multi-coupled systems, with and without damping, *J. Sound Vib.* **40** (1975) 19–39.
18. D. J. Mead, Wave propagation in continuous periodic structures: research contributions from Southampton, 1964–1995, *J. Sound Vib.* **190** (1996) 495–524.
19. F. Romeo and A. Luongo, Invariants representation of propagation properties for bi-coupled periodic structures, *J. Sound Vib.* **257** (2002) 869–886.
20. M. Brun, G. F. Giaccu, A. B. Movchan and L. I. Slepyan, Transition wave in the collapse of the San Saba Bridge, *Front. Mater.* **1** (2014) 12.
21. F. Maurin and A. Spadoni, Wave dispersion in periodic post-buckled structures, *J. Sound Vib.* **333** (2014) 4562–4578.
22. G. Carta and M. Brun, Bloch-Floquet waves in flexural systems with continuous and discrete elements, *Mech. Mat.* **87** (2015) 11–26.
23. L. I. Slepyan, M. V. Ayzenberg-Stepanenko and G.S. Mishuris, Forerunning mode transition in a continuous waveguide, *J. Mech. Phys. Solids* **78** (2015) 32–45.
24. A. J. Hull, A higher-order shear deformation model of a periodically sectioned plate, *J. Vib. Acoust.* **138** (2016) 051010.
25. M. J. Nieves, G. S. Mishuris and L. I. Slepyan, Analysis of dynamic damage propagation in discrete beam structures, *Int. J. Solids Struct.* **97–98** (2016) 699–713.

26. S. G. Haslinger, N. V. Movchan, A. B. Movchan, I. S. Jones and R. V. Craster, Controlling flexural waves in semi-infinite platonic crystals with resonator-type scatterers, *Q. J. Mech. Appl. Math.* **70** (2017) 216–247.
27. G. M. T. D’Eleuterio and P. C. Hughes, Dynamics of gyroelastic continua, *J. Appl. Mech.* **51** (1984) 415–422.
28. P. C. Hughes and G. M. T. D’Eleuterio, Modal parameter analysis of gyroelastic continua, *J. Appl. Mech.* **53** (1986) 918–924.
29. G. M. T. D’Eleuterio, On the theory of gyroelasticity, *J. Appl. Mech.* **55** (1988) 488–489.
30. K. Yamanaka, G. R. Heppler and K. Huseyin, Stability of gyroelastic beams, *AIAA J.* **34** (1996) 1270–1278.
31. S. Hassanpour and G. R. Heppler, Theory of micropolar gyroelastic continua, *Acta Mech.* **227** (2016) 1469–1491.
32. S. Hassanpour and G. R. Heppler, Dynamics of 3D Timoshenko gyroelastic beams with large attitude changes for the gyros, *Acta Astron.* **118** (2016) 33–48.
33. G. Carta, I. S. Jones, N. V. Movchan, A. B. Movchan and M. J. Nieves, Gyro-elastic beams for the vibration reduction of long flexural systems, *Proc. Math. Phys. Eng. Sci.* **473** (2017) 20170136.
34. G. Carta, A. B. Movchan, L. P. Argani and O. S. Bursi, Quasi-periodicity and multi-scale resonators for the reduction of seismic vibrations in fluid-solid systems, *Int. J. Eng. Sci.* **109** (2016) 216–239.
35. H. Goldstein, C. Poole and J. Safko, *Classical Mechanics*, 3rd edn., (Addison Wesley, San Francisco 2002).
36. K. F. Graff, *Wave Motion in Elastic Solids*, 1st edn., (Dover Publications Inc., New York 1975).
37. R. A. Diaz, W. J. Herrera and R. Martinez, Moments of inertia for solids of revolution and variational methods, *Eur. J. Phys.* **27** (2006) 183–192.
38. G. Floquet, Sur les équations différentielles linéaires à coefficients périodiques, *Ann. Sci. École Norm. Sup.* **12** (1883) 47–88.
39. F. Bloch, Über die Quantenmechanik der Elektronen in Kristallgittern, *Zeit. Physik* **52** (1928) 555–600.
40. L. Brillouin, *Wave Propagation in Periodic Structures: Electric Filters and Crystal Lattices*, 1st edn., (McGraw-Hill, New York 1946).
41. M. Brun, A. B. Movchan and L. I. Slepyan, Transition wave in a supported heavy beam, *J. Mech. Phys. Solids* **61** (2013) 2067–2085.
42. G. Carta, G. F. Giaccu and M. Brun, A phononic band gap model for long bridges. The ‘Brabau’ bridge case, *Eng. Struct.* **140** (2017) 66–76.

## APPENDIX

### A. Massless beam with a clamped end and a gyro-hinge

Here we study a massless beam, whose eigenfrequencies are finite in number and can be expressed in closed form. The boundary conditions are the same as in section 4.1, namely the beam is clamped at one end and possesses a gyro-hinge at the other end. When  $\rho = 0$ , Eq. (4.4) takes the following form:

$$\left(4EJ - I_0 I \omega^2\right)^2 - I^2 l^2 \omega^2 \Omega^2 = 0, \quad (\text{A.1})$$

whose four solutions are given by

$$\omega_{1,2} = \frac{\pm I\sqrt{l}\Omega + \sqrt{16EJ I_0 + I^2 l \Omega^2}}{2I_0\sqrt{l}}, \quad (\text{A.2a})$$

$$\omega_{3,4} = \frac{\pm I\sqrt{l}\Omega - \sqrt{16EJ I_0 + I^2 l \Omega^2}}{2I_0\sqrt{l}}. \quad (\text{A.2b})$$

For any value of the gyricity  $\Omega$ , either positive or negative, all the four solutions (A.2) are real and, in particular,  $\omega_1, \omega_2 > 0$  while  $\omega_3, \omega_4 < 0$ .

We illustrate the results for the special case of a cylindrical gyroscopic spinner, considered in Section 5. Fig. A1a is a three-dimensional representation of the functions  $\omega_{1,2} = \omega_{1,2}(I/I_0, \Omega)$ , while Figs. A1b,c and A1d,e are cross-sections of Fig. A1a at specific values of  $\Omega$  and  $I/I_0$  respectively, as indicated in the figure.

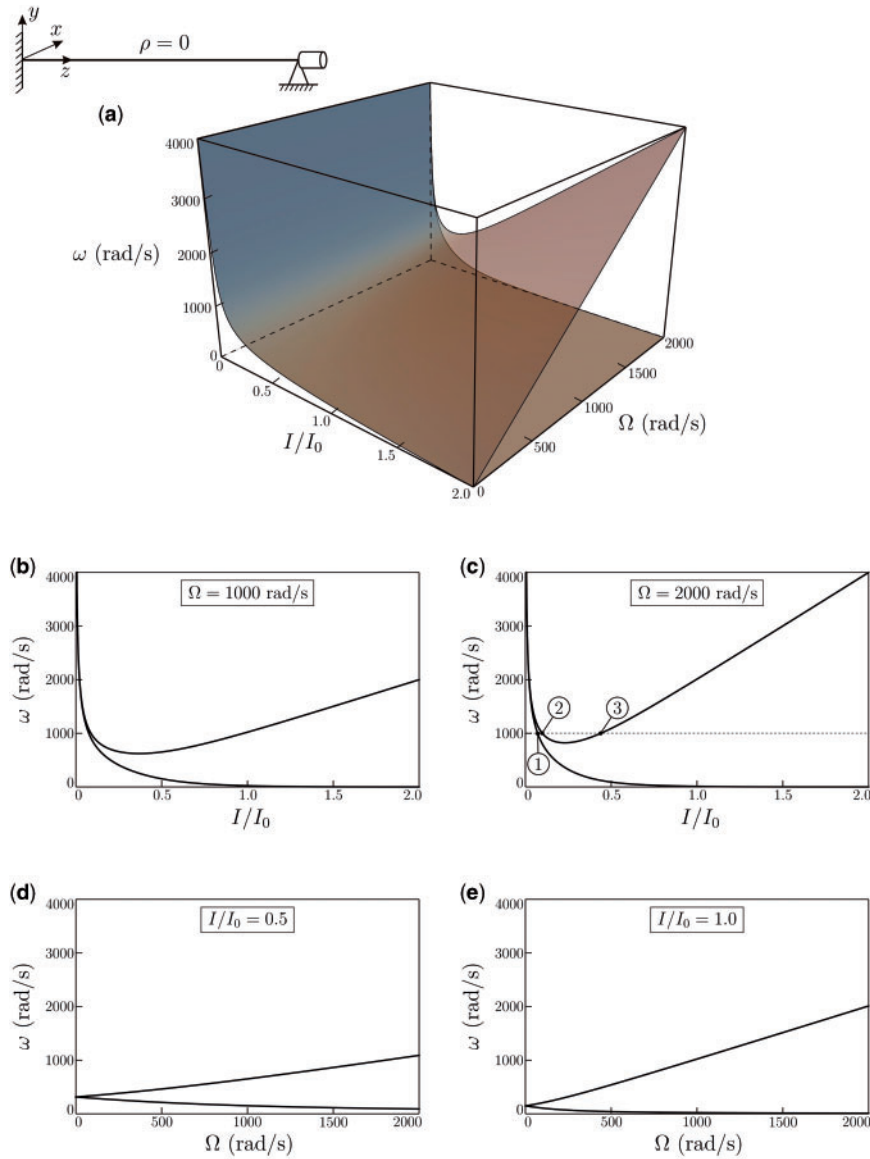
For a fixed value of  $\Omega$  (Figs. A1b and A1c), we note that one eigenfrequency decreases monotonically with increasing  $I/I_0$ , while the other one presents a minimum. The two curves have no intersections for  $I/I_0 > 0$ . It is interesting to observe that in the limit when  $I/I_0 \rightarrow 2$ ,  $\omega_1$  tends to a finite value different from zero, while  $\omega_2 \rightarrow 0^+$  (when  $\Omega > 0$ , while for  $\Omega < 0$   $\omega_1$  and  $\omega_2$  are swapped). By introducing a small positive parameter  $\epsilon = 2 - I/I_0$  ( $0 < \epsilon \ll 1$ ), we can write the following asymptotic approximation for  $\omega_1$  and  $\omega_2$ :

$$\omega_1 \sim 2\Omega, \quad \omega_2 \sim \frac{3EJ}{m_{\text{cyl}}h_{\text{cyl}}^2 I \Omega} \epsilon \quad \text{when} \quad \epsilon = 2 - \frac{I}{I_0} \rightarrow 0, \quad (\text{A.3})$$

where  $m_{\text{cyl}}$  and  $h_{\text{cyl}}$  are the mass and the height of the cylindrical gyroscopic spinner, respectively.

For a fixed value of  $I/I_0$  (Figs. A1d and A1e), the two eigenfrequencies depend on  $\Omega$  monotonically, with one being an increasing function of  $\Omega$  and the other being a decreasing function. The only intersection of the graphs of these functions is found at  $\Omega = 0$  and it represents a double eigenfrequency.

The time-harmonic motions of the beam in correspondence with the three eigenfrequencies indicated by numbers ‘1’ to ‘3’ in Fig. A1c, equal to  $\omega = 1000$  rad/s and obtained for  $\Omega = 2000$  rad/s, are displayed in the videos included in the Supplementary Material. We point out that the beam rotates in the clockwise direction at the eigenfrequency denoted by ‘1’ in Fig. A1c, while it rotates in the counter-clockwise direction at the eigenfrequencies labelled as ‘2’ and ‘3’.



**Fig. A1** (a) Eigenfrequencies of a massless beam with a clamped end and a gyro-hinged end for different values of the ratio  $I/I_0$  and of the gyricity  $\Omega$ ; cross-sections of (a) at different values of  $\Omega$ : (b)  $\Omega = 1000$  rad/s, (c)  $\Omega = 2000$  rad/s; cross-sections of (a) at different values of  $I/I_0$ : (d)  $I/I_0 = 0.5$ , (e)  $I/I_0 = 1.0$ . In these computations, the spinner has a cylindrical shape